Infrared Spectroscopy and Analysis of Brown Dwarf and Planetary Mass Objects in the Orion Nebula Cluster

D. J. Weights[1]⋆, P. W. Lucas[1], P. F. Roche[2], D. J. Pinfield[1], F. Riddick[2]

[1] *Dept of physical sciences, University of Hertfordshire, College Lane, Hatfield Al10 9AB, England.*
[2] *Astrophysics Dept, University of Oxford, 1 Keble Road, Oxford, OX1 3RH, England.*

20 October 2008

ABSTRACT

We present near-infrared long slit and multi-slit spectra of low mass brown dwarf candidates in the Orion Nebula Cluster. The long slit data were observed in the *H*- & *K*-bands using NIRI on the Gemini North Telescope. The multi-object spectroscopic observations were made using IRIS2 on the Anglo Australian Telescope at *H*-band. We develop a spectral typing scheme based on optically calibrated, near infrared spectra of young sources in the Taurus and IC 348 star forming regions with spectral types M3.0 to M9.5. We apply our spectral typing scheme to 52 sources, including previously published UKIRT and GNIRS spectra. 40 objects show strong water absorption with spectral types of M3 to >M9.5. The latest type objects are provisionally classified as early L types. We plot our sources on H-R diagrams overlaid with theoretical pre-main-sequence isochrones. The majority of our objects lie close to or above the 1 Myr isochrone, leading to an average cluster age that is <1 Myr. We find 38 sources lie at or below the hydrogen burning limit (0.075 $M_\odot$). 10 sources potentially have masses below the deuterium burning limit (0.012 $M_\odot$). We use a Monte Carlo approach to model the observed luminosity function with a variety of cluster age and mass distributions. The lowest χ^2 values are produced by an age distribution centred at 1 Myr, with a mass function that declines at sub-stellar masses according to an M^α power law in the range α=0.3 to 0.6. We find that truncating the mass function at 0.012 $M_\odot$ produces luminosity functions that are starved of the faintest magnitudes, even when using bimodal age populations that contain 10 Myr old sources. The results of these Monte Carlo simulations therefore support the existence of a planetary mass population in the ONC.

Key words: stars: low-mass, brown dwarfs - stars: formation - stars: mass function, luminosity function - stars: pre-main-sequence

1 INTRODUCTION

The characterisation of the brown dwarf and planetary mass populations in star forming regions is important in order to measure the Initial Mass Function (IMF) and to learn whether the timing and duration of the formation process changes at low masses. Young clusters are amongst the best locations to probe the substellar IMF because young brown dwarfs are several orders of magnitude brighter than mature field brown dwarfs.

The Orion Nebula Cluster (ONC) is an excellent location to search for brown dwarfs and planetary mass objects. Extensive research demonstrates that the cluster is extremely young with an average age of ⩽1Myr (e.g. Prosser et al. 1994; Hillenbrand 1997, Palla & Stahler 1999; Riddick,

Roche & Lucas (2007, hereafter RRL)). The cluster is also nearby (∼450pc (Luhman et al. 2000)), permitting us to probe for sources with masses below the hydrogen burning limit. The dense background of the OMC-1 cloud and relatively high galactic latitude ($b = -19°$) minimise contamination from background stars (Hillenbrand & Hartmann 1998).

In recent years deep near-infrared studies of young clusters have led to the detection of large numbers of brown dwarf and planetary mass candidates (Comeron et al. 1993; Williams et al. 1995; Lucas & Roche 2000; Lucas, Roche & Tamura 2005). The luminosity and colour criteria (see Section 2 for more details) used for differentiating between sub-stellar and higher mass cluster members have proven to be successful, with spectroscopic follow-up confirming the existence of significant numbers of brown dwarfs in Orion

⋆ E-mail: d.j.weights@herts.ac.uk

and other star-forming regions (Lucas et al. 2001; Luhman et al. 2003; Meeus & McCaughrean 2005).

Despite spectroscopic confirmation of a large number of brown dwarfs, a considerable fraction of potentially low-mass cluster members remain uncharacterised. Spectroscopy has demonstrated that we cannot rely on photometry alone to determine the nature of objects. Samples are subject to contamination from both foreground and reddened background stars. Photometric parameters can be skewed by scattering of light from dust and circumstellar material. In addition to this, theoretical pre-main-sequence models become less certain at young ages. Spectroscopic observations are therefore critical to accurately calibrate the physical properties of young objects and determine the true nature of the initial mass function (IMF) and luminosity function (LF) below the hydrogen burning limit.

Measurements of the low mass IMF are useful to inform and constrain the theory of star formation as a whole. By characterising the nature of the IMF in different environments we can establish whether it is universal. The associated mapping of the spatial distribution of low and high mass sources which may also improve star formation theory.

This work extends our previous spectroscopic studies to a larger sample in order to analyse the substellar mass function and age distribution. We analyse low resolution near-infrared *H*- and *K*-band spectroscopic observations of 55 brown dwarf candidates in the ONC. In Section 2 we describe the observations and the data reduction process. We present our *H*- and *K*-band spectra in Section 3. In Section 4 we describe the spectral typing scheme that was developed for our different data sets and present the results. H-R diagrams are used to to determine source mass in the following section. Here we discuss the results from the H-R diagram and implications on cluster age. In our penultimate section we show results of Monte Carlo modelling of the LF. We experiment with different mass functions and age distributions and see how these parameters effect the LF. Our modelling sheds light on the initial conditions that are most likely in the ONC and how a population of planetary mass objects effect the LF.

2 OBSERVATIONS

Near-infrared spectra of Orion brown dwarf candidates were obtained in classical observing mode at two epochs, each using a different observational technique. The first data were acquired using the Near InfraRed Imager (NIRI) on the 8-m Gemini North Telescope over the period 5-8 December 2003. Objects in this dataset were observed through a single slit. The second data-set was obtained with the Anglo Australian Telescope (AAT) using the Infrared Imager and Spectrograph (IRIS2, see Tinney et al. 2004). These observations were carried out during 20-25 November 2004. With the implementation of high astrometric precision masks, the instrument was operated as a multiple-slit spectrograph.

Candidate sources were selected for observation from UKIRT photometry of Lucas et al. 2000 & Lucas et al. 2001 and from Gemini South/Flamingos photometry of Lucas, Roche and Tamura 2005. All sources had prospective masses ranging from below the hydrogen burning limit ($\lesssim$ 75M$_{Jup}$) down close to the deuterium burning limit ($\sim$ 13M$_{Jup}$; as-

suming solar metalicity). The main selection criteria were identical for both data sets; however, subtle differences in the selection strategy were required due to the capabilities and limitations of each instrument and telescope. The critical requirements were as follows: (1) Sources were avoided that were close to or embedded in bright nebulosity. For optimum sensitivity objects were chosen that were located in regions of low nebula surface brightness. (2) Sources were only chosen if they possessed fairly low extinction values (A$_V$ $\lesssim$7.5). (3) Candidates that were in a resolved close binary system were avoided.

In total 16 of the 17 brown dwarf candidate spectra observed with NIRI were useful. 4 of these objects do not appear in this paper as they were published in paper 1 (Lucas et al. 2006). A sample of 44 targets were observed with the AAT using IRIS2, 17 of which were brown dwarf candidates and of sufficient quality to be of scientific value. 2 of these objects were observed by chance due to coincidental slit alignment. Table 1 lists photometric properties, total integration times and the observed waveband(s) for each source. Dereddened *H*-band magnitudes have been tabulated as they are referred to throughout the paper. Emphasis has been put on objects that were not on our target list and were observed by chance.

The observations in the NIRI data set were carried out using the f/6 camera in conjunction with the 1024×1024 pixel ALADDIN InSb array. This combination yielded a scale of 0.117 arcsec per pixel. Efficiency was maximised by simultaneously observing closely spaced candidate sources in pairs. The spectra were observed with a 0.7 arcsec slit with a resolving power of R=520. A data acquisition sequence consisting of two nod positions (ABBA pattern) separated by 3 arcsec was employed. This allowed the removal of the dark current and near perfect removal of telluric OH emission and emission from nebulosity. All of the candidates in this data set were observed with the *K*-band grism. Two pairs were also observed with the *H*-band grism. Flat fields were taken at the beginning of each evening and morning using the Gemini Calibration unit (GCAL). Stellar standards were observed throughout each night at a similar airmass to each of the sources. The UKIRT list of faint standards was used to carefully choose F- and G-type stars prior to the observing run. An Argon lamp was used to create several arc images each night. The observing conditions were photometric on three of the four nights. The observations on 6th December were cut short due to cloud.

The observations with IRIS2 employed cryogenically cooled slit masks, an observing mode which had not been fully commissioned at the time. With the implementation of two different masks, a total of 44 brown dwarf candidates were observed. The detector used was a 1024×1024 Rockwell HgCdTe Hawaii array. A scale of 0.4487 arcsec per pixel provided a field of view of 7.7 arcmin^2. Brown dwarf candidates were selected for observation that had apparent magnitudes brighter than mag 17 at *H*- band. Each mask contained holes for four bright fiducial stars that were used to precisely align the telescope to the correct field. In an attempt to remove the telluric OH emission the data were again acquired using an ABBA nod pattern. The nod distance was experimented with in order to maximise the number of sources that appeared in their relative slit in both nod positions. Several candidates in each field only had a spectrum visible in one

nod position. This problem was encountered for approximately two sources in each mask. Both masks were observed with a *J*-long (1.10−1.33 μm) and an *H*-short (1.46−1.81 μm) grism with integration times ranging between 3 and 4 hours.

Standard stars were observed throughout each night using an unorthodox method to illuminate all the slits in each mask. The standard star was defocused until it illuminated two or three adjacent slits. Then a fast chopping mode of the telescope was used to further spread out the image profile so that several adjacent slits were illuminated simultaneously. By repeating this method three or four times a calibration spectrum could be taken through every slit in a mask.

Flat fields and Xe arcs were taken at the beginning of each night through each filter and each mask. Three of the six nights allocated for observing were abandoned due to bad weather. The data from the remaining three clear nights had fairly poor seeing (typically > 1.6 arcsec) that was variable on short timescales.

Erratum

We would like to point out a naming error in Lucas et al. 2006 (paper 1). The spectrum plotted for 022-115 is actually the *K*-band spectrum of 023-1939. Both objects are reddened background stars, with similar spectral profiles. We include the spectral typing results of 022-115 in this paper.

2.1 Data Reduction

Both single slit and multiple slit data were reduced using IRAF software.

Standard techniques were used to reduce the NIRI long slit data. For each brown dwarf candidate pair, exposures were separated into their relative nod positions (A or B). Groups A and B were median combined separately using the IMCOMBINE task in IRAF. One combined image pair was then subtracted from the next, removing the dark current and most of the background. An argon arc was used to wavelength calibrate the data. Each image was wavelength calibrated and corrected for distortion using the IDENTIFY, REIDENTIFY, FITCOORDS and TRANSFORM routines in IRAF. All spectra were extracted using APALL. The residual background that remained after subtraction was removed during the extraction using two background software apertures adjacent to the target spectrum. Telluric standards were created from standard stars that had been divided by a blackbody representing the temperature of the associated stellar spectral type. Spectra were cleaned in order to remove spurious noise spikes, residual OH lines, nebula lines and any remaining residual background features. Extracted pairs from each nod position were coadded and finally dereddened using the DEREDDEN task in IRAF, with an adopted reddening parameter of 3.1.

2.2 IRIS2 Reduction Techniques

The initial reduction steps of combining and subtracting pairs was carried out in the manner described above. Poor observing conditions meant that the combined images contained a significant amount of residual background caused by very short timescale variable telluric OH. Shorter exposure times were experimented with at the telescope but

were inadequate for checking the position of spectra. Due to the nature of Multi-Object Spectroscopy (MOS) the subtracted images could not be wavelength calibrated and rectified for distortions in the manner described above. Instead spectra were extracted individually with APALL. The trace was recorded and used again to extract a Xenon arc from the same position in the relative slit. This was sufficient for wavelength calibration due to the fact that geometric distortions were insignificant. A master telluric standard was constructed for each mask rather than a separate standard star for each individual slit. To achieve full wavelength coverage the standard stars were observed through the furthermost left and right slits and a central slit. We checked that this approach was appropriate by comparing an extracted spectrum from each slit. By dividing each spectrum by the next we were able to demonstrate that the throughput did not change from slit to slit. The telluric standard was created in the same manner described in Section 2.1. Each object spectrum was divided by the master telluric standard. Cleaning, coadding and dereddening procedures were as described above. Due to the lateral variation of slit positions in the masks used for multiple object spectroscopy, the final wavelength coverage of each spectrum is different.

3 SPECTROSCOPY

3.1 *H*-Band

The *H*-band spectra of objects observed with IRIS2 and NIRI, that show H_2O absorption and have sufficient signal to noise to be spectral typed are presented in Figure 1. We also plot the spectrum of 047-436. This object has a red continuum and shows no H_2O absorption. All spectra are plotted as F_λ with a flux scale normalised at 1.68 μm. Spectra from our sample that had a Rayleigh-Jeans type continuum were not plotted. The distinctive triangular peak that is ubiquitous in young low surface gravity objects (Lucas et al. 2001), due to strong H_2O absorption and pressure sensitive H_2 absorption, can be seen in each of the spectra close to 1.675 μm. None of the ONC objects reveal obvious narrow features that are unassociated with the pixel to pixel noise fluctuations. The plots do not demonstrate the complete wavelength coverage of each spectrum due to the fact that telluric noise begins to increase dramatically outside this spectral range for most of our Orion spectra. Many of the IRIS2 spectra have low signal to noise and have subsequently been smoothed for clarity. The quality of the AAT spectra drops towards the edges of the atmospheric window due to the low altitude of the observatory so absorption longward of 1.72 μm may be masked by noise. Careful observation of 047-436 reveals a steep gradient between 1.68 and 1.72 μm may exist. However, without improved spectral coverage this remains uncertain. Despite the low signal to noise in the spectrum of 031-536 the pseudo continuum shows convincing evidence of strong water absorption. The spectroscopic data becomes unreliable shortward of 1.59 μm where the noise significantly increases. Spectral data is absent at wavelengths shorter than 1.55 μm for 024-124 due to limited wavelength coverage.

5th order cubic splines have been fitted to each of the spectra. The continuum fits were created using a fitting procedure within SPLOT, in IRAF. To ensure a high quality

Table 1. Photometric data and total integration times for sources from the IRIS2 and NIRI data sets that are presented in this paper. Objects that could not be spectral typed due to insufficient signal to noise have not been included. Photometric data is from Lucas & Roche (2000) and Lucas et al.(2001;2005).

Source[a]	Data Set	J	H	H_{dr}	K	A_v	Integration Time (min) H- , K-
010-109	NIRI	17.39	16.37	15.55	—	4.67	— , 186
011-027	IRIS2	15.55	14.99	14.95	—	0.25	200 , —
013-306	NIRI	16.90	15.61	14.37	14.63	7.06	— , 40
015-319	NIRI	18.08	17.26	16.78	16.49	4.26	— , 40
020-1946	IRIS2 & NIRI	16.48	15.35	14.39	—	5.47	110 , 112[b]
023-1939	NIRI	18.87	17.98	17.46	—	3.01	— , 112
024-124[c]	IRIS2	14.32	13.33	12.70	—	3.60	200 , —
030-524	NIRI	17.86	17.40	17.40	16.77	0.00	— , 60
031-536	IRIS2	16.72	16.23	16.23	15.52	0.00	200 , —
044-527	NIRI	17.38	16.88	16.88	16.18	0.00	— , 60
047-245	IRIS2	17.27	16.62	16.41	16.10	1.23	110 , —
047-436	IRIS2	15.61	14.37	13.28	12.64	6.22	110 , —
053-323	IRIS2	15.98	15.43	15.39	15.15	0.25	110 , —
056-141	IRIS2	17.34	16.34	15.54	—	4.54	200 , —
057-305	IRIS2	17.31	15.61	13.75	14.81	10.66	110 , —
067-651	IRIS2	15.78	14.95	14.46	—	2.78	110 , —
077-453	IRIS2	13.90	13.10	12.76	12.79	1.93	200 , —
084-104	NIRI	17.42	16.89	16.88	—	0.05	— , 32
087-024	IRIS2	16.60	15.56	14.74	—	4.67	110 , —
095-058	NIRI	13.71	13.25	13.25	—	0.00	— , 32
121-434	IRIS2	14.51	13.43	12.66	—	4.44	200 , —
127-044[c]	IRIS2	13.67	13.19	13.19	—	0.00	110 , —
130-053	IRIS2	15.77	15.20	15.12	—	0.44	200 , —
186-631	NIRI	15.94	15.28	15.07	14.58	2.27	52 , 180
192-723	NIRI	17.11	16.08	15.27	15.41	4.64	34 , 124
196-659	NIRI	17.85	17.00	16.44	16.34	3.20	— , 130
235-454	IRIS2	14.84	13.82	13.11	—	4.06	228 , —
255-512	IRIS2	17.11	16.10	15.31	—	4.50	228 , —

Notes:
[a] Source names are coordinate based, following O'Dell & Wong (1996).
[b] *H*-band data was from IRIS2 and *K*-band was from NIRI.
[c] Source was observed in the slit by chance.

fit could be established, each spectrum was first box-car smoothed using an 11 pixel size box and trimmed to give a wavelength range limited between 1.50 and 1.675 µm. The cubic spline fits represent the pseudo continuum satisfactorily, avoiding spurious narrow structures in the spectra that are a due to noise. The cubic spline fits were constructed to provide us with a robust reference for spectral typing (see section 4).

The IRIS2 *H*-band source 047-436 has a red continuum that has no strong H_2O absorption. 047-436 is a deeply embedded cluster member which displays strong H_2 emission lines in its *K*-band spectrum and strong CaII emission lines in its optical spectrum (Lucas et al. 2001; RRL). We have plotted the spectrum of this object as F_ν so that the reader can make a direct comparison of the two spectra. Between 1.58 and 1.79 µm we measure a rise in relative flux that is marginally less than observed by Lucas et al. 2001. The difference in this slope is probably due to the fact that we dereddened our spectrum based on a larger A_v estimate. Shortward of 1.58 µm our spectrum is approximately flat. This contrasts with the previously published *H*-band spectrum where the gradient of the pseudo continuum is constant over the entire wavelength range. We believe that this

difference may be attributed to the combination of the low signal to noise present in our spectrum and the fact that the shortest wavelength region is at the edge of the array for this object. The spectral profile of 047-436 changes significantly when converted to an F_λ flux scale, presenting a pseudo continuum that gently declines between 1.50 and 1.60 µm and then proceeds to remain flat until 1.80 µm. The spectrum is not characteristic of a young, low mass cluster member. However, Lucas et al. 2001 demonstrated that this object showed signs of youth at *K*-band and is a definite cluster member. The photometry of this object reveals an anomalously blue $(I-J)$ colour $((I-J)=3.21)$ suggesting the source is associated with circumstellar matter. The slope of the dereddened spectrum may therefore be unreliable due to the fact that scattered light is causing us to overestimate the flux at shorter wavelengths. Due to potential water absorption being veiled by extinction we are unable to determine whether this object is a low mass star or a brown dwarf. This object may be a proto-brown dwarf or a background star that has been dereddened inaccurately.

We have not plotted the *H*-band spectrum of 057-305 despite reasonable signal to noise. The spectrum of this object is similar to that of 047-436, showing a red continuum

when displayed as F_ν and a flat spectrum when plotted as F_λ. The extinction to this this object is relatively high (A_v=10.662) thus no *I*-band detection has been attained. Due to the fact that there is no *I*-band photometry for this source and we do not have a *K*-band spectrum, we cannot determine whether this object is a cluster member or background star.

3.2 *K*-Band

NIRI *K*-band spectra are presented in Figure 2. Only objects that were of high enough quality to be spectral typed have been shown. Spectra that had a Rayleigh-Jeans type continuum were not plotted. For consistency the wavelength coverage in the plots ranges between 1.96 and 2.36 µm. This does not represent the entire wavelength coverage and has been done due to some spectra having very poor signal to noise beyond this range. The spectra are plotted using a normalised F_λ flux scale. The pseudo continuum of each spectrum has been fit by a 6th order cubic spline that has been over-plotted in all cases. The continuum fits were created using the same procedure described for the *H*-band spectra. The spectra were smoothed with an 11 pixel boxcar and trimmed to give a wavelength range of 1.96 to 2.36 µm. Not every spectrum in the sample required this much smoothing or trimming. However, the same parameters were used on each object for consistency. Smoothing by this amount may dilute narrow lines such as CO and NaI. However, these are not required for the spectral typing procedure. The final fits followed the pseudo-continuum very well and were used for spectral typing.

The shape of the water absorption profile can be seen in a similar configuration as observed at *H*-band, with a flux peak close to 2.20 µm. The flux maxima are flatter than seen at *H*-band, producing a spectral profile that is less obviously triangular in shape. All spectra show strong absorption beyond this wavelength suggesting that water absorption is not significantly veiled by hot circumstellar dust. Three of the ten spectra presented at *K*-band (010-109, 095-058 and 186-631) show evidence of the first ($\nu = 2-0$) vibration-rotation bandhead of CO at 2.295 µm, a feature often seen to be weak in young objects. The spectra of 095-058 and 186-631 show clear evidence of multiple CO bandheads. Figure 3 shows 186-631 with extended wavelength coverage out to 2.46 µm. Multiple CO bandheads can be seen at 2.32, 2.35 and 2.38 µm. All of these vibration-rotation absorption features can be seen in the spectrum 095-058. A further three spectra show weak evidence of the 2.295 µm CO absorption feature; 013-306, 015-319 and 084-104. It is possible that the tentative CO absorption feature seen in 084-104 at 2.295 µm is attributable to noise. The spectra of 186-631 and 095-058 appear to be somewhat different to the other *K*-band spectra. The spectra of 095-058 and 186-631 peak at a longer wavelength than the 2.2 µm peaks of the other young objects, at a wavelength of ∼2.26 µm. This is not an artifact introduced by noise as the signal to noise for these spectra are relatively high. Empirical evidence in numerous publications suggests this is not abnormal for young objects and is in fact commonly observed; e.g. Luhman, Peterson & Megeath 2004, Luhman et al. 2005, Luhman et al. 2006. Both 044-527 and 030-524 have low signal to noise and have been smoothed. Despite low signal to noise the spectral profile of 044-527

appears to be consistent with that of a young, low gravity object. The cubic spline fit represents the pseudo-continuum for this object well and is therefore suitable for spectral typing. The *K*-band spectrum of 030-524 is less convincing due to the low signal to noise. However, this object is a probable low mass cluster member. RRL have obtained a high quality spectrum for this object at optical wavelengths. From the data they derive a spectral type of M7.5±1.5. This indicates that the broad H2O absorption bands depicted by the cubic spline fit are likely to be genuine.

4 SPECTRAL TYPING

Accurate spectral typing is critical if we want to have a good understanding of the true behavior of the IMF at the sub-stellar regime. Until recently the spectral classification of low mass objects in young stellar nurseries was determined via the use of spectral indices that were empirically derived from a variety of field brown dwarf and giant spectra combinations e.g. the optical work carried out in IC 348 by Luhman et al.(2003). Comparisons with synthetic spectra created from detailed theoretical model calculations (e.g. D'Antona & Mazzitelli, 1997 (hereafter DM97); Baraffe et al. 1998; Chabrier et al. 2000 and Allard, Hauschildt & Schwenke, 2000) have also been used to spectral type objects and derive intrinsic temperatures. For the evolved population of field dwarfs these techniques are an excellent tool for spectral classification, yielding accurate results. However, significant limitations exist when applying these techniques to very young objects. Infrared spectral indices that compare relative strengths of molecular and atomic features observed in field dwarfs, often fail to predict a real spectral type as might be defined at optical wavelengths (Lucas et al.2001). This is due to the fact that near-infrared indices are predominantly assigned to gravity sensitive features that dominate the spectra. The very young brown dwarf and planetary mass candidates found in Orion are still at an early stage in their evolution and thus are still contracting and have large radii. The consequential low surface gravity results in broad water absorption bands that are suppressed by collision induced H_2 absorption in more evolved high surface gravity field dwarfs (Kirkpatrick et al. 2006). The v=2−0 vibration-rotation bands of CO starting at 2.29 µm are weaker in absorption in young, late M-type sources, seemingly due to gravity differences. However, veiling of warm circumstellar dust may also contribute. As a consequence of these physical differences, spectral indices will often predict spectral types that are too late. Theoretical models become uncertain at ages below 1 MYr and thus should be avoided as a sole tool for accurate spectral typing.

In order to ascertain accurate spectral types of young objects with the use of empirical measurements, indices must be derived and calibrated from similar objects of known spectral type. Until recently this has been difficult to do for young substellar objects due to the lack of high quality optical spectra for near-infrared counterparts. High quality infrared spectra of 39 young (∼1 - 2 Myr) objects ranging in spectral type from M3 to M9.5 were kindly supplied by Kevin Luhman (original spectra can be seen in Briceño et al. 2002; Luhman et al. 2003b; Luhman 2004). These are located in Taurus and IC 348 star forming regions. The
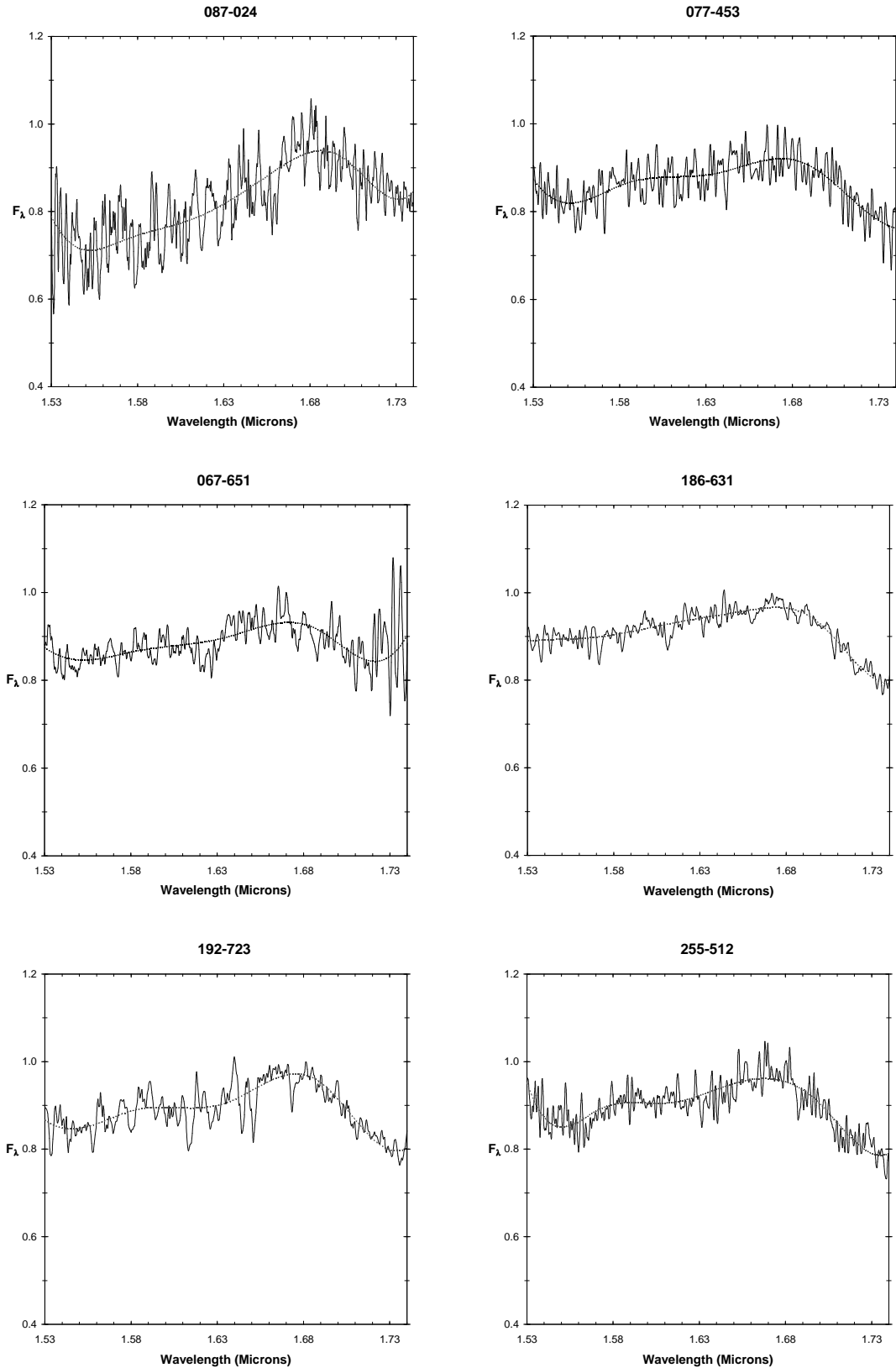
Figure 1. Normalised, dereddened *H*-band IRIS2 and NIRI spectra. Each source shows strong H_2O absorption, resulting in a triangular spectral profile. This provides strong evidence that the objects are young and have low surface gravity. The spectral resolution is too low to resolve narrow features. Therefore the noise is indicated by the pixel to pixel variations. A 5th order cubic spline fit is overplotted onto each spectrum. Note that the spectrum of 047-436 is plotted as F_ν
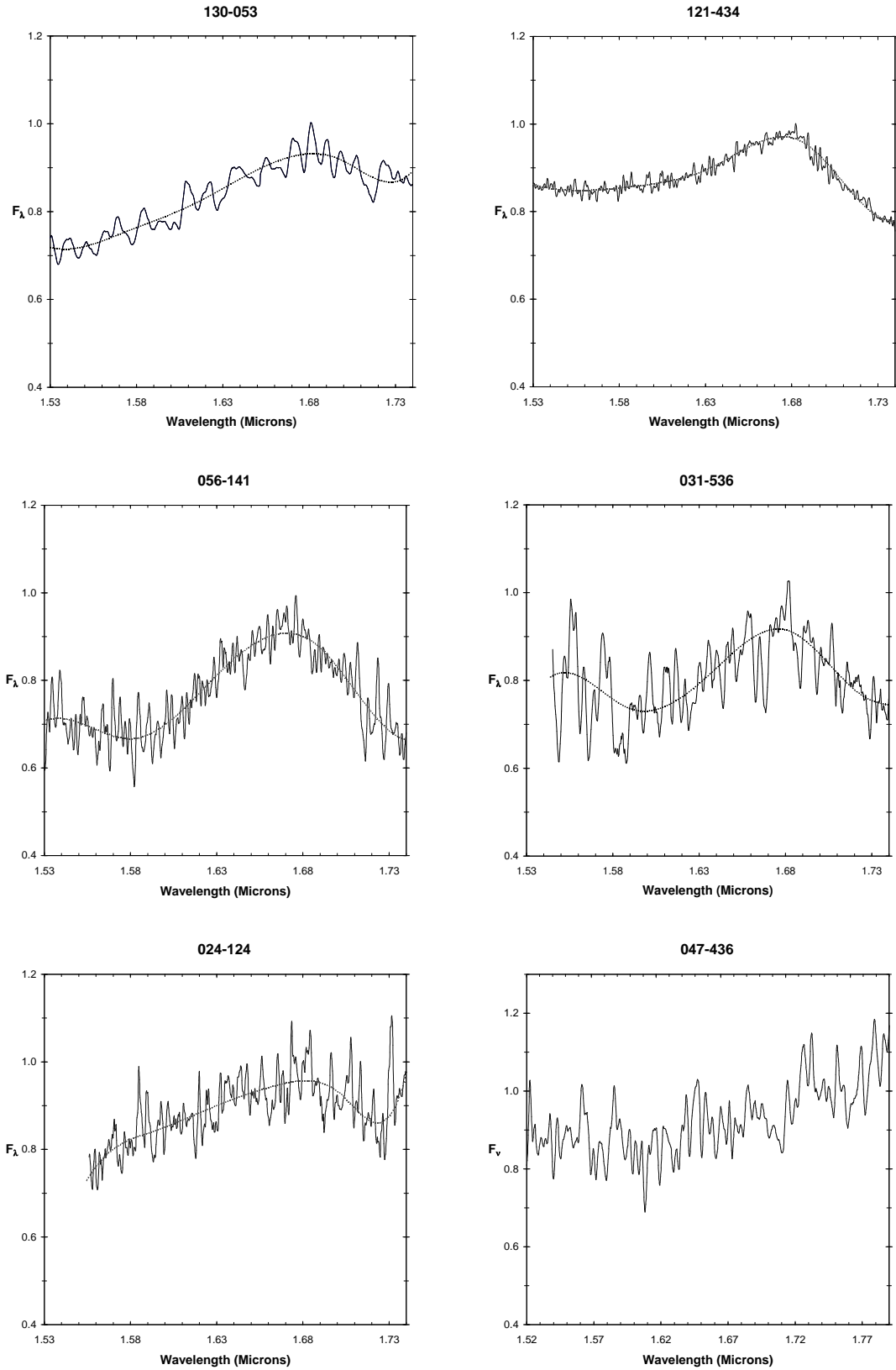
130-053

121-434

056-141

031-536

024-124

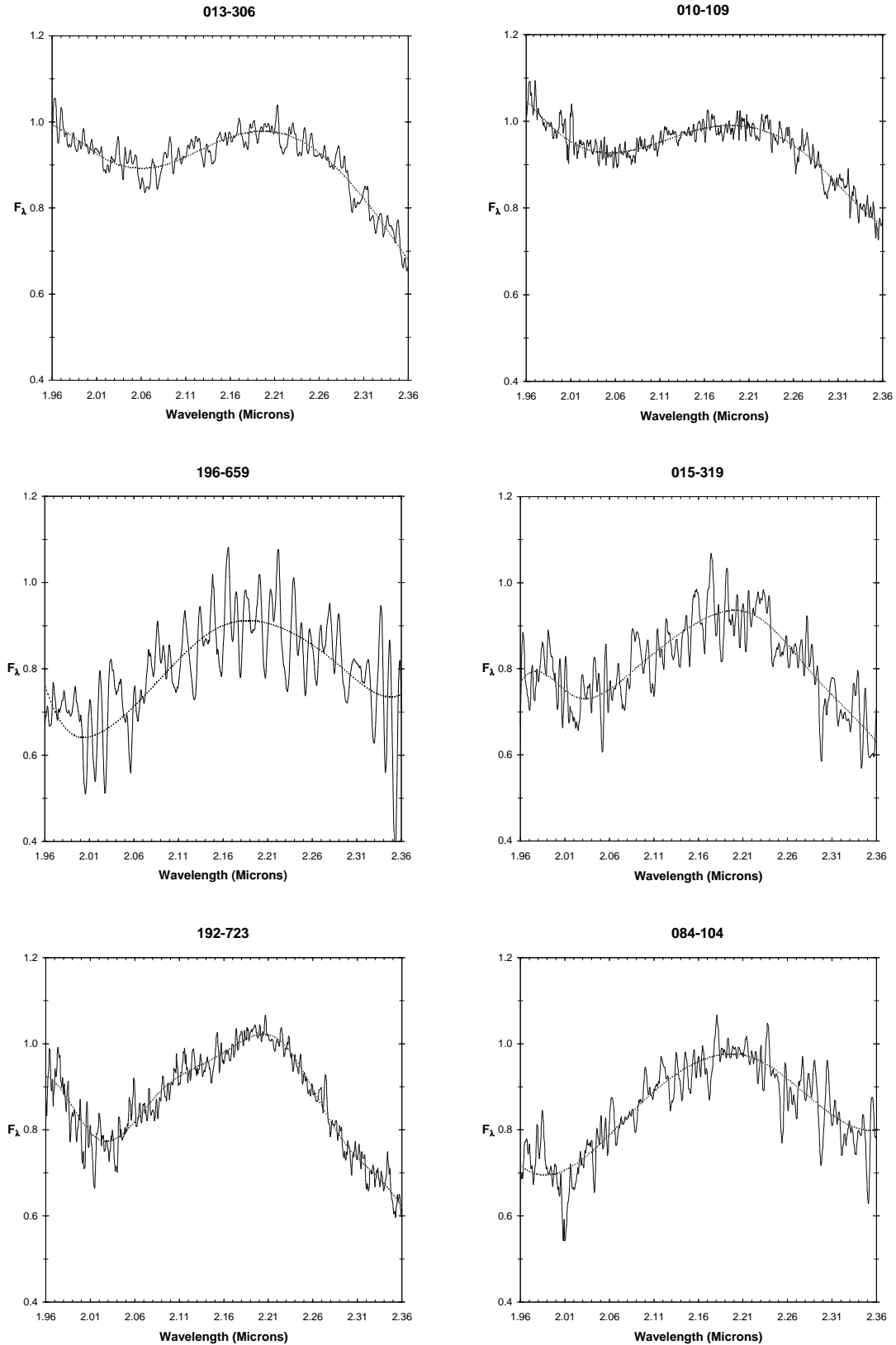**047-436**

Figure 1. continued

Figure 2. Normalised, dereddened K-band NIRI spectra. Each source shows strong H_2O absorption, resulting in a flat-peaked, triangular spectral profile. This provides strong evidence that the objects are young and have low surface gravity. Several spectra show evidence of CO absorption at 2.295 μm. The 6th order cubic spline fit to the continua used for spectral typing has been overplotted onto each spectrum.
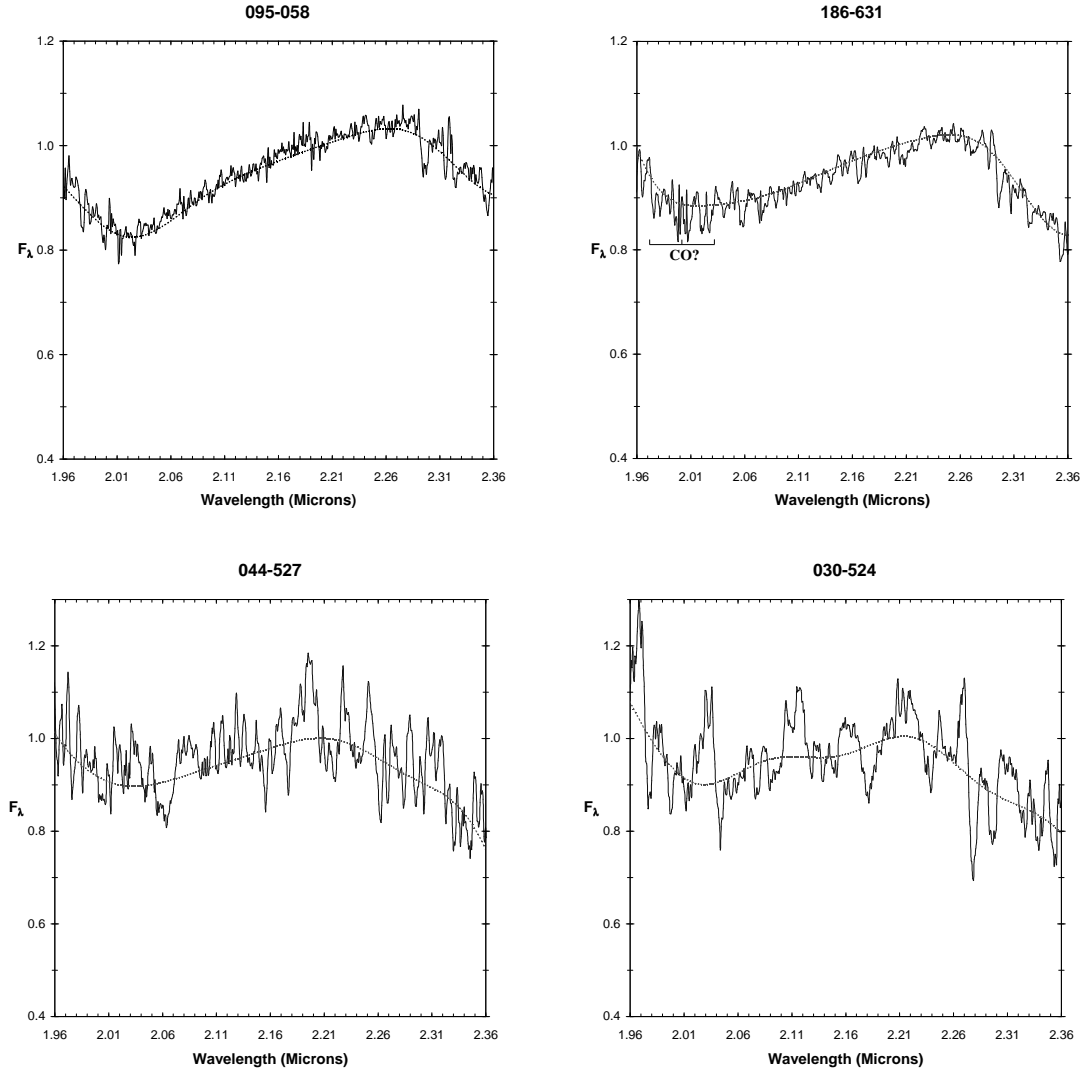
Figure 2. continued

low resolution (R=100) spectra were obtained with SpeX on IRTF. The spectral types for these objects were calibrated from high quality optical spectra and are therefore reliable for calibration. All spectra are F_λ and had been corrected for reddening. RRL have optically determined spectral types for 17 ONC sources in our infrared sample, 9 of which were observed at infrared wavelengths by Lucas et al. 2001. The 8 additional sources have been covered by our sample here. We chose to use Luhman's sample only when deriving spectral types. This is because the quality of his template spectra were generally of higher quality and thus more reliable than ours.

A total of four indices were constructed to spectral type each of the Orion brown dwarf candidates. These differ slightly from those mentioned in the previous paper (Lucas et al. 2006) as they required careful adjustment in order for them to satisfy the spectral coverage in the IRIS2 and NIRI spectra. Each index measures the strength of the water absorption bands. The F_λ flux value was determined by the median flux in a 0.02μm wide interval centered on the de-

sired wavelength. Flux ratios were plotted as a function of spectral type for each object in the Luhman sample. A fit was derived for each spectral index using a cubic polynomial. The polynomial fits are not weighted as the true error for each data point cannot be quantified accurately. If systematic errors are neglected we can approximate an error using the internal scatter within the finite wavelength regions applicable to the spectral index. Pseudo errors were generated for Luhman's data, for each index, and then used to generate weighted fits. Due to the smooth nature of Luhman's low resolution spectra, the weighted fits showed an insignificant difference to the non-weighted fits, implying that our approach is reliable, provided systematic errors are small.

The index ratios that were chosen had to satisfy two requirements. Firstly the quality of the fit should be high (i.e. coefficient of determination ($R^2 > 0.9$ where possible). R^2 is the coefficient of determination and is shown in Equation 1. The numerator represents the sum of the squared errors and the denominator represents the total sum of the squares. y_i represents a data value, $\hat{y_i}$ represents a model value and $\bar{y}$
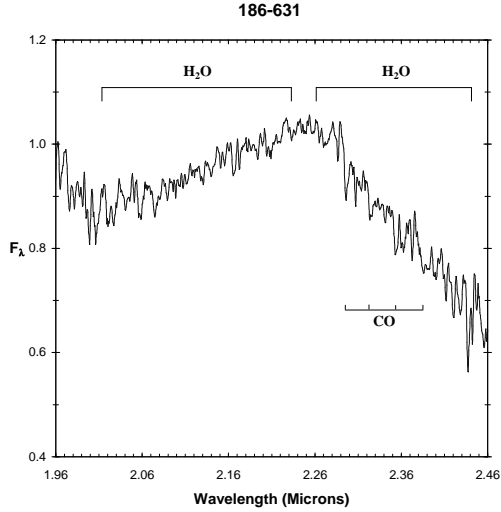
Figure 3. Strong H_2O absorption can be seen either side of a peak situated close to 2.26 μm. The triangular profile indicates that the object has low surface gravity and is therefore young. Multiple band heads of CO can be seen at 2.29, 2.32, 2.35 and 2.38 μm.

is the mean of the data values. Secondly the gradient of the fit should not be too shallow so that a small error in a given index will not result in a significant span of spectral types. Index ratios were rejected if they produced a fit that was too shallow regardless of how good the fit was. The four indices are defined in Equations 2 to 5.

$$R^2 = 1 - \frac{\sum\limits_{i}(y_i - \hat{y}_i)^2}{\sum\limits_{i}(y_i - \bar{y})^2} \tag{1}$$

$$WH = \frac{F_\lambda(1.562\mu m)}{F_\lambda(1.665\mu m)} \tag{2}$$

$$WK = \frac{F_\lambda(2.050\mu m)}{F_\lambda(2.190\mu m)} \tag{3}$$

$$QH = \frac{F_\lambda(1.562\mu m)}{F_\lambda(1.665\mu m)} \left[\frac{F_\lambda(1.740\mu m)}{F_\lambda(1.665\mu m)}\right]^{1.581} \tag{4}$$

$$QK = \frac{F_\lambda(2.050\mu m)}{F_\lambda(2.192\mu m)} \left[\frac{F_\lambda(2.340\mu m)}{F_\lambda(2.192\mu m)}\right]^{1.140} \tag{5}$$

The QH and QK indices (Equations 4 and 5) are a reddening independent measurement of water absorption, assuming the Cardelli, Clayton & Mathis (1989) reddening law of $\lambda^{-1.61}$. To ensure errors were minimal, these indices were constructed so that the two wavelength regions either side of the central wavelength position were approximately equidistant, i.e. keeping the exponents close to unity. The QH index was not used on all the *H*-band data. This was because the spectral coverage on the right hand side of the triangular peak, seen close to 1.68 μm, was not always available. It is also important to note that for most of the AAT spectra that had sufficient wavelength coverage, the noise increased heavily as the wavelength approached the edge of

the *H*-band atmospheric transmission window; thus rendering these wavelength regions unreliable for spectral typing. The WH and WK indices measure the strength of the water absorbtion on the shorter side of the flux peak in each waveband. Due to the fact that these indices are not reddening independent, any inaccuracies in the derived A_V values for an object will result in a small error in the determined index. However, these indices are still useful and provide robust spectral types for each object. This is particularly true for the WK index as it is less affected by possible veiling due to hot circumstellar dust seen beyond 2.2 μm. We find that altering A_V values by ±2 changes the derived spectral type by less than 0.5 in the majority of cases. The spectral indices described above are illustrated in Figure 4. The fit parameters are summarised in Table 2. Meaningful errors could not be assigned to the each cubic polynomial coefficient and constant term because the errors in Luhman's data are unquantifiable.

A further set of spectral indices were created to re-analyse an existing *H*- and *K*-band data set of young ONC objects. The data were obtained at UKIRT in November 1999, and previously published in Lucas et al. (2001). At the time of publication few optically calibrated young brown dwarf spectra existed. As a result of this, spectral types were calibrated from indices applied to evolved field dwarfs, consequently leading to over-estimated spectral types.

Both W and Q indices were constructed for the *H*- and *K*-band UKIRT data. Due to the fact that the UKIRT *H*-band data had greater wavelength coverage to the IRIS2 data, the preferential WH index described in paper 1 (Lucas et al. 2006) was selected for analysis. Minor adjustments were required for the WK, QH and QK indices described in paper 1, and the WK and QK indices used with the IRIS2 and NIRI data in this paper. Each new index was created based on the criteria described earlier in this section. The indices that were used for spectral typing the UKIRT data can be seen in Equations 6 to 9, and are represented graphically in Figure B1 in Appendix B1. For clarity, the names of the indices associated with the UKIRT data have been appended with the subscripted letters 'UK' in parenthesis. The fit parameters for of the UKIRT indices are summarised in Table 2. The QH and $QH_{(UK)}$ indices are reasonably insensitive beyond M 7.5 due to the cubic polynomial fits being fairly flat beyond this point.

$$WH_{(UK)} = \frac{F_\lambda(1.525\mu m)}{F_\lambda(1.675\mu m)} \tag{6}$$

$$WK_{(UK)} = \frac{F_\lambda(2.080\mu m)}{F_\lambda(2.190\mu m)} \tag{7}$$

$$QH_{(UK)} = \frac{F_\lambda(1.530\mu m)}{F_\lambda(1.670\mu m)} \left[\frac{F_\lambda(1.780\mu m)}{F_\lambda(1.670\mu m)}\right]^{1.551} \tag{8}$$

$$QK_{(UK)} = \frac{F_\lambda(2.080\mu m)}{F_\lambda(2.192\mu m)} \left[\frac{F_\lambda(2.345\mu m)}{F_\lambda(2.192\mu m)}\right]^{0.830} \tag{9}$$

The GNIRS indices (except WH_G) from paper 1 are represented in Figure B2 in Appendix B2. The fit parameters associated with these objects are presented in Table 2. These data were not included in the original publication.

Indices that were applicable to the spectral data were used with the solutions to their corresponding cubic polynomial fits, to determine a spectral type. Indices were run on
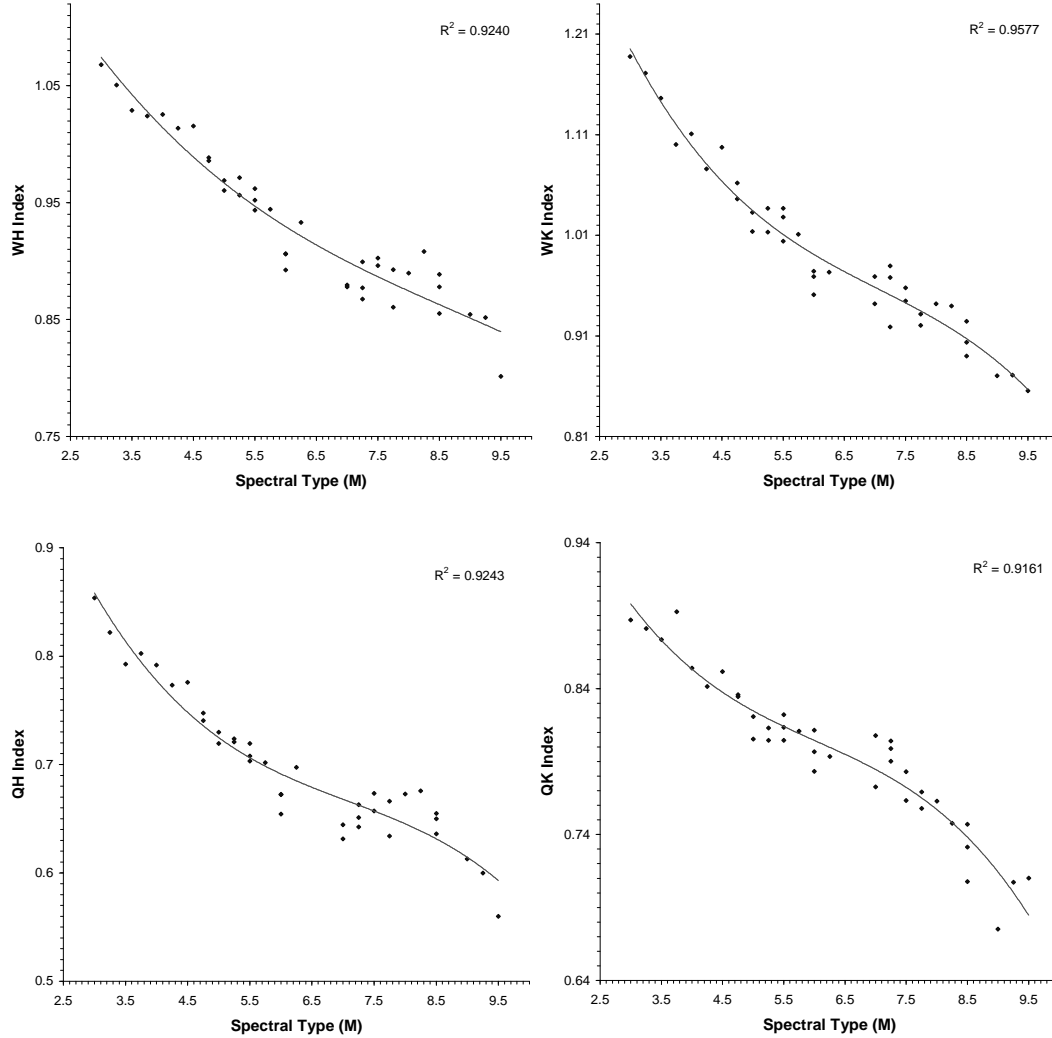
Figure 4. Index strength as a function of spectral type. Each data point represents an object from Luhman's near-infrared spectroscopic sample of optically calibrated young (∼1Myr) brown dwarfs. For each ratio the median flux value in a 0.02μm interval was used. The relationship between spectral type and index are fitted by cubic polynomials. The R^2 values are correlation coefficients (see Section 4 for details.).

Table 2. Parameters for cubic polynomial fits to the indices associated with the IRIS2 and NIRI data from this work, the UKIRT data from Lucas et al. 2001 and the GNIRS data in paper 1. The parameters for the $WH_{(G)}$ index are not listed as they are identical to those of the $WH_{(UK)}$. The precision of each coefficient is supplied to allow accurate spectral typing. However, using the 3rd and 2nd order terms to this accuracy only should be adequate. The R^2 values represent the correlation coefficient (see Section 4 for details.).

Index Name	αx^3	βx^2	γx	Const.	R^2
WH	−0.0004533128	0.0118652078	−0.1265391170	1.3595251240	0.9240
WK	−0.0017114928	0.0362490654	−0.2866080191	1.7754365826	0.9577
QH	−0.0015340095	0.0326200036	−0.2526304540	1.3626402514	0.9243
QK	−0.0013174804	0.0239071298	−0.1633687914	1.2085945875	0.9161
$WH_{(UK)}$	−0.0007842812	0.0177687976	−0.1770229758	1.5162233490	0.9453
$WK_{(UK)}$	−0.0012965703	0.0279422070	−0.2225218246	1.5852276527	0.9449
$QH_{(UK)}$	−0.0013136355	0.0309180885	−0.2698736864	1.3226247704	0.9276
$QK_{(UK)}$	−0.0012109998	0.0229457232	−0.1598483183	1.2099851645	0.8974
$WK_{(G)}$	−0.0019817649	0.0442701944	−0.3617322968	1.9892775060	0.9520
$QH_{(G)}$	−0.0011389261	0.0260481258	−0.2218064454	1.2761433125	0.9137
$QK_{(G)}$	−0.0009214824	0.0159583585	−0.1151253304	1.1080547649	0.9261

the cubic spline fits to take into account the poor signal to noise inherent to most of the data. The final spectral typing results were derived using the solutions from all applicable indices in most cases. If a pseudo continuum fit did not represent the data well in a wavelength region required for a particular index, the result was discarded. When data quality was clearly superior at one wavelength, more weight was given to the spectral types derived from indices using the same passband. Spectral types were rounded to the nearest 0.5 sub-type.

All results from the spectral typing procedure were checked by over-plotting template spectra from Luhman's sample. Several objects observed at *H*- and *K*-band had spectra that appeared to be later in one of the observed wavebands (see Section 4.1 for details). Over-plotting template spectra confirmed these measurements, demonstrating that the discrepancy was not due to a weakness in spectral index. In the cases where the difference in spectral type was not obviously due to poor data quality, the final type was derived using an average.

011-027 has poor spectral coverage at the blue end of the *H*-band spectrum because of its location on the array. Due to the fact that there is no spectral information at 1.562 μm we could not use our indices to type this object. Instead we over-plotted a selection of template spectra from Luhman's sample and calibrated the object by visual inspection. 011-027 is not plotted in Figure 1 as it has a Rayleigh-Jeans type continuum. The spectrum of 031-536 has adequate spectral coverage but was not spectral typed using our indices. This is because the spectrum rises, becoming more noisy in the wavelength region around 1.562 μm that is required for spectral typing. The apparent rise in flux is due to increasing noise towards the edge of array. The *H*-band profile beyond 1.60 μm is triangular in shape, showing strong water absorption either side of the peak seen close to 1.68 μm. The pseudo continuum fit follows the noise in this region and therefore results in a generated spectral type that is too early if indices are used. To overcome this problem we have visually typed this object by over plotting a selection of template spectra. Due to the fact the spectrum of 031-536 is noisy and unreliable at $\lambda > 1.60$ μm we assign a large error to the spectral type.

4.1   Spectral Typing Results

Table 3 shows the final spectral types that were calculated for each object and summarises the indices used to determine these values. The GNIRS data from Lucas et al. 2006 has also been included in the Table 3. 12 of the sources had H_2O absorption that was stronger than that of any object in Luhman's sample. These objects were assigned spectral types '> M9.5' because we cannot trust that the cubic polynomial fits are valid for objects later than this. These 12 sources, together with 5 objects that have derived spectral types of M9.5 and $\geqslant$ M9.5 are shown below the dotted line in Table 3. Five sources have a steep Rayleigh-Jeans type continuum and appear hotter than the warmest object (M 3.0) in Luhman's sample of template spectra. A further 7 sources had spectral profiles representative of objects ranging from M3.0 to M4.5 in the template sample. All 12 early M-type sources are likely to be foreground stars or reddened background stars. We confirmed this by plotting

the sources on an H-R diagram combined with pre-main-sequence isochrones (see section 5 for details). All sources lie below the 50 Myr isochrone, demonstrating that they do not belong to the cluster. Due to the fact that these objects are not ∼1Myr old cluster members, the derived spectral types are invalid. In addition to this, the A_v values derived from the colour-magnitude diagram will be incorrect. Non cluster members are separated in Table 3 by a solid line. We loosely classify these objects as 'early M'.

For the highest quality data the results generated from the different indices agreed well, typically to within 1 spectral type. However, in a few cases results differed by up to 2 spectral types. The significant anomalies in determined spectral type (i.e. discrepancies >1.5) have been carefully scrutinised. The anomalies are discussed in Appendix A.

The spectral typing method that we have used makes it hard to determine a robust error for each of the indices. This is because we cannot accurately determine the error in the cubic spline fit at the wavelength intervals used for each index. In addition, we cannot quantify the error in the spectral types assigned to the template spectra. A visual inspection indicated the cubic spline fits represented the data well at wavelengths critical for spectral typing (a spectral index was avoided if this was not the case). The error in spectral type was subsequently derived using the scatter in the results. This was then increased to account for systematic errors. The standard error of the mean (standard deviation $/ \sqrt{n}$) was used to determine the error in spectral type. This value was then increased by half a sub-type to take into account further errors. The errors in Table 3 have been rounded to the nearest half sub-type. For sources with spectral types based on a single measurement the error was estimated based on the signal to noise of the data. Errors have been neglected for objects that appear later than M9.5 and for reddened background stars.

The effective temperatures in Table 3 were determined using the revised temperature scale of Luhman et al. (2003). The temperature scale was constructed for young sources (∼ 2 Myr) in the IC 348 star forming region. It is therefore a suitable approximation for the youthful objects in the ONC. The errors in effective temperature are somewhat unquantifiable due to the absence of uncertainties in the spectral type to effective temperature scale. We have assigned errors to the derived effective temperatures based on the error in spectral type. Because the temperature scale is not defined beyond M9, upper limits have been assigned to objects later than M9. Because the Luhman temperature scale is not defined beyond M9, upper limits have not been assigned to objects >M9. We have not attempted to derive effective temperatures for sources we believe to be background stars. This is because our spectral typing scheme is calibrated from very young objects and is not designed for evolved main sequence stars.

5   H-R DIAGRAM

In Figure 5 we present H-R diagrams for the full sample of sources with infrared spectra from this work and from Lucas et al.(2001) and Lucas et al.(2006). Classically, an H-R diagram is plotted with bolometric luminosity on the y-axis. We have plotted dereddened *H*-band magnitude rather than

Table 3. Final spectral types for all sources with sufficient signal to noise to be spectral typed (including GNIRS and NIRI data from paper 1). Spectral types derived from UKIRT and GNIRS indices are subscripted by (UK) and (G), respectively. 17 sources have water absorption that is stronger than or equal to that of the coolest object in Luhman's template data set. These appear below the dotted line in the table. 13 sources have spectra that show a smoothly declining Rayleigh-Jeans tail. These are probably reddened background stars and are shown below the solid line in the bottom section of the table. Source 047-436 is a proplyd and has therefore been excluded from this table.

Source[a]	Data Set	H_{dr}	WH[b]	WK[b]	QH[b]	QK[b]	Final Type	T_{eff}(K)[c]	$M/M_\odot$[d]
010-109	NIRI	15.55	——	7.7	——	8.7	M8.0±0.75	2710^{+127}_{-232}	$0.030^{+0.020}_{-0.017}$
013-306	NIRI & UKIRT	14.37	$9.1_{(UK)}$	9.0	$7.7_{(UK)}$	9.9	M9.0±0.75	2400^{+232}	$0.014^{+0.010}$
014-413	UKIRT	14.16	$8.1_{(UK)}$	$8.4_{(UK)}$	$5.9_{(UK)}$	$6.1_{(UK)}{}^e$	M7.5±0.75	2795^{+112}_{-317}	$0.040^{+0.025}_{-0.018}$
016-410	UKIRT	12.23	$4.2_{(UK)}$	——	$5.8_{(UK)}$	——	M5.0±1.00	3125^{+145}_{-135}	$0.150^{+0.025}_{-0.050}$
016-430[g]	GNIRS	18.64	11.5	$10.7_{(G)}$	$9.3_{(G)}$	$6.4_{(G)}$	M9.0±2.00	2400^{+480}	$0.014^{+0.046}$
019-354	UKIRT	13.81	$5.7_{(UK)}$	$7.5_{(UK)}$	$5.2_{(UK)}$	$8.0_{(UK)}$	M6.5±1.00	2935^{+122}_{-140}	$0.075^{+0.045}_{-0.035}$
030-524	NIRI	17.40	——	7.8	——	7.9	M8.0±0.75	2710^{+127}_{-233}	$0.040^{+0.025}_{-0.025}$
043-014	UKIRT	13.76	$8.0_{(UK)}$	——	$7.6_{(UK)}$	——	M8.0±0.25	2710^{+42}_{-77}	$0.030^{+0.005}_{-0.005}$
044-527	NIRI	16.88	——	8.6	——	8.5	M8.5±0.50	2555^{+155}_{-155}	$0.024^{+0.004}_{-0.005}$
053-503	UKIRT	13.57	$7.5_{(UK)}$	$7.9_{(UK)}$	——	$6.6_{(UK)}$	M7.5±0.50	2795^{+85}_{-85}	$0.040^{+0.030}_{-0.020}$
067-651	IRIS2	14.46	6.1	——	——	——	M6.0±0.75	2990^{+101}_{-82}	$0.082^{+0.030}_{-0.017}$
068-019	UKIRT	13.73	$5.7_{(UK)}$	$7.9_{(UK)}$	$5.7_{(UK)}$	$7.7_{(UK)}$	M7.0±0.75	2880^{+82}_{-127}	$0.060^{+0.030}_{-0.025}$
069-209	UKIRT	13.67	$5.7_{(UK)}$	$9.8_{(UK)}{}^e$	$5.8_{(UK)}$	$7.6_{(UK)}{}^e$	M6.0±0.50	$2990^{+67.5}_{-55}$	$0.090^{+0.022}_{-0.025}$
077-453	IRIS2	12.76	6.2	——	——	——	M6.0±0.75	2990^{+101}_{-82}	$0.082^{+0.030}_{-0.030}$
084-1939	UKIRT	14.78	$9.8_{(UK)}$	$9.3_{(UK)}$	$8.8_{(UK)}$	$8.9_{(UK)}$	M9.0±0.25	2400^{+77}	$0.014^{+0.002}$
091-017[f]	UKIRT	13.68	$4.3_{(UK)}$	$4.5_{(UK)}$	$4.5_{(UK)}$	$3.4_{(UK)}$	M4.5±0.50	3198^{+72}_{-72}	$0.157^{+0.060}_{-0.032}$
092-532[g]	GNIRS	17.50	9.8	$7.5_{(G)}$	$5.0_{(G)}$	$3.9_{(G)}$	M7.5±2.00	2795^{+263}	$0.040^{+0.028}$
095-058	NIRI & UKIRT	13.25	$7.4_{(UK)}$	9.6	$6.5_{(UK)}$	6.9^e	M7.5±0.75	2795^{+112}_{-162}	$0.040^{+0.025}_{-0.015}$
096-1943	UKIRT	14.75	$8.5_{(UK)}$	$9.4_{(UK)}$	——	——	M9.0±0.50	2400^{+155}	$0.014^{+0.006}$
107-453[g]	GNIRS	18.66	8.6	$4.7_{(G)}$	$9.6_{(G)}$	$5.6_{(G)}$	M8.0±2.00	2710^{+280}	$0.030^{+0.052}$
121-434	IRIS2	12.66	6.9	——	7.0	——	M7.0±0.25	2880^{+27}_{-42}	$0.060^{+0.010}_{-0.010}$
186-631	NIRI	15.07	5.9	8.7	5.8	8.2	M7.0±1.00	2880^{+110}_{-170}	$0.058^{+0.030}_{-0.030}$
255-512	IRIS2	15.31	6.3	——	6.8	——	M6.5±0.50	2935^{+55}_{-55}	$0.065^{+0.015}_{-0.023}$
015-319	NIRI & UKIRT	16.78	$11.5_{(UK)}$	10.2	$7.8_{(UK)}$	10.9	>M9.5	<2400	<0.014
024-124	IRIS2	12.70	10.7	——	——	——	>M9.5[f]	<2400	<0.014
031-536	IRIS2	16.23	——	——	——	——	M9.5±1.50[f]	<2400	<0.014
037-628	UKIRT	17.18	$9.4_{(UK)}$	——	$10.4_{(UK)}$	——	>M9.5	<2400	<0.014
055-230	UKIRT	13.11	$9.4_{(UK)}$	$10.1_{(UK)}$	$9.1_{(UK)}$	$10.0_{(UK)}$	M9.5±0.5	<2400	<0.014
056-141	IRIS2	15.54	12.5	——	——	——	>M9.5	<2400	<0.014
057-247[g]	GNIRS	18.49	8.8	$9.3_{(G)}$	$10.1_{(G)}$	$10.0_{(G)}$	≥M9.5[f]	<2400	<0.014
061-400	UKIRT	17.71	$10.5_{(UK)}$	——	$10.0_{(UK)}$	——	>M9.5	<2400	<0.014
084-104	NIRI & UKIRT	16.88	$11.1_{(UK)}$	10.6	$10.6_{(UK)}$	10.1	>M9.5	<2400	<0.014
087-024	IRIS2	14.74	9.7	——	——	——	M9.5±0.75	<2400	<0.014
130-053	IRIS2	15.12	11.2	——	——	——	>M9.5	<2400	<0.014
137-532[g]	GNIRS	17.14	10.9	$9.2_{(G)}$	$10.0_{(G)}$	$9.2_{(G)}$	>M9.5	<2400	<0.014
152-717[g]	GNIRS	17.74	9.3	$10.3_{(G)}$	$10.2_{(G)}$	$9.2_{(G)}$	>M9.5	<2400	<0.014
183-729[g]	GNIRS	17.15	7.6	$10.6_{(G)}$	$10.0_{(G)}$	$10.2_{(G)}$	≥M9.5[f]	<2400	<0.014
188-658[g]	GNIRS	18.60	9.7	$9.5_{(G)}$	$10.7_{(G)}$	$10.5_{(G)}$	>M9.5	<2400	<0.014
192-723	NIRI	15.27	9.3	$9.4_{(G)}$	——	$10.7_{(G)}$	>M9.5	<2400	<0.014
196-659	NIRI	16.44	——	$10.2_{(G)}$	——	$10.2_{(G)}$	>M9.5	<2400	<0.014
011-027	IRIS2	14.95	——	——	——	——	Early M[f]	——	——
019-108	UKIRT	13.56	——	——	——	——	Early M	——	——
020-1946	IRIS2 & NIRI	14.39	——	——	——	——	Early M	——	——
022-115	NIRI	18.07	——	——	——	——	Early M	——	——
023-1939[g]	NIRI	17.46	——	——	——	——	Early M	——	——
047-245	IRIS2	16.41	——	——	——	——	Early M	——	——
053-323	IRIS2	15.39	——	——	——	——	Early M	——	——
057-305	IRIS2	13.75	——	——	——	——	Early M	——	——
127-044	IRIS2	13.19	——	——	——	——	Early M	——	——
199-617[g]	NIRI	18.04	——	——	——	——	Early M	——	——
205-610[g]	NIRI	17.62	——	——	——	——	Early M	——	——
235-454	IRIS2	13.11	——	——	——	——	Early M	——	——

Notes:
[a] Source names are coordinate based, following O'Dell & Wong (1996).
[b] Spectral types that were derived using the UKIRT indices have been appended by the subscripted letters 'UK' in parenthesis.
[c] These quantities were derived using spectral type to effective temperature scale of Luhman (2003)
[d] Masses were determined from an H-R diagram (see Section 5.2 for details).
[e] This result was not used to derive the final spectral type.
[f] Spectral type was determined by over-plotting template spectra.
[g] Source from paper 1 (Lucas et al. 2006)

bolometric luminosity in order to avoid the uncertainties associated with converting to a bolometric magnitude. The upper panel of Figure 5 has overlaid theoretical models of the Lyon group, while the lower panel has overlaid models from DM97. The plots in the upper panel use different Lyon group models in different temperature ranges. The DUSTY models (Allard et al.2001) have been used at $T_{eff} < 2500$ K (the temperature at which dust begins to become important) and the NEXTGen models (Baraffe et al.1998; Chabrier et al.2000) have been used at $T_{eff} > 2500$ K. For the coolest objects ($T_{eff} < 1800$K) we use the magnitudes predicted by the DUSTY models but adopt the colours of field dwarfs, as the DUSTY models are known to be too red at such low temperatures (Chabrier et al. 2000). The highest mass sources in the 1 and 3 Myr dusty isochrones required a 0.15 mag shift in the H-band to ensure a seamless join to the NextGen isochrones.

The fluxes in the NextGen and Dusty models are presented in the CIT format. They were converted to the MKO system using appropriate filter transformation equations[1]. The absolute magnitudes of each object were converted to apparent magnitudes using the distance modulus equation with an assumed distance to Orion of 450 pc. The DM97 model data provided bolometric luminosity only. To account for this we derived our own bolometric correction at H-band based on the models by the Lyon Group. Two approaches were experimented with, each giving results that were similar. The first approach generated bolometric corrections by comparing relative masses between the models. For objects of the same mass, H-band magnitudes in the Lyon models were subtracted from the bolometric luminosities presented in the DM97 models to give a bolometric correction. Where similar masses were not available linear interpolation was used to derive a correction. The second corrections were calculated from temperature comparisons using a similar technique. Although the final discrepancies in the results from the two procedures were small, the method based on temperature comparisons was used. This is because bolometric corrections directly relate to temperature and are therefore a more sensible choice.

In Figure 5 the UKIRT data from Lucas et al. 2001 appear as diamonds, the IRIS2 and NIRI data are shown as triangles and the GNIRS data from Lucas et al. 2006 are displayed as squares. Sources that had derived spectral types later than M9.0 are plotted as as upper limits. Objects whose spectra are represented by obvious Rayleigh-Jeans tails are not likely to be cluster members and have been excluded from the plots. The errors in dereddened H-band magnitude are dominated by photometric uncertainties. The

derivation of errors in effective temperature is described in Section 4.1. In general the error in effective temperature increases as spectral type becomes later. The IRIS2 object 013-306, GNIRS object 107-453 and UKIRT objects 084-1939 & 096-1943 have constrained spectral types within the optically classified range of the Luhman sample. Due to the magnitude of the errors for these sources and an absence in temperature data beyond M9.0, error bars could only be included for higher effective temperatures. Upper limits were used for lower effective temperatures. In each plot the mass track of the hydrogen burning limit ($0.075M_\odot$) has been highlighted as a bold dotted line.

5.1 Analysis

For objects with effective temperatures > 2500K the 1Myr isochrone of the DM97 model appears to trace the observed data quite well. However, Luhman et al. (2003) used empirical isochrones to show that the pre main sequence NextGen and Ames Dusty models agree well with observational constraints for low mass sources. The DM97 models have less detailed physics and assume gray atmospheres which, are thought to be an inappropriate approximation for stars whose effective temperatures fall below 4500K (Baraffe et al. 1998). Thus, the NextGen and Ames Dusty models are regarded as more reliable and robust than those of DM97. Both H-R Diagrams in Figure 5 show a considerable number of sources that lie above the 1 Myr isochrone. This is more noticeable with the NextGen and Dusty models. Although the error bars can account for the scatter of most objects above the youngest isochrones, both models suggest a population of objects that are younger than 1 Myr. This is a particularly interesting result as it is in agreement with results by Slesnick, Hillenbrand & Carpenter (2004, hereafter SHC04) and RRL. Some of these objects may not necessarily be younger than 1 Myr in age and may in fact represent unresolved binary systems. If the binary systems comprise objects of similar luminosity, the components in question will be ~0.75 magnitudes fainter, moving them significantly closer to the 1 Myr isochrones. The true binary fraction in Orion is unknown. Recent studies (e.g. Reipurth et al. 2007) suggest the overall binary fraction is 8.8% ±1.1%, a factor of ~1.5 less than seen in the field. The binary fraction of the low mass population in the central part of the ONC is comparable to that seen in the field (e.g. Padgett, Strom & Ghez 1997; Simon, Close & Beck 1999; Köler et al. 2006). Ongoing research is helping to refine this measurement (e.g Irwin et al. 2007; Cargile, Stassun & Mathieu 2008). Binarity may therefore explain some of the observed scatter.

Interestingly, several objects lie below the 5 Myr isochrone and close to the 10 Myr isochrone in both diagrams suggesting they may be associated with an earlier
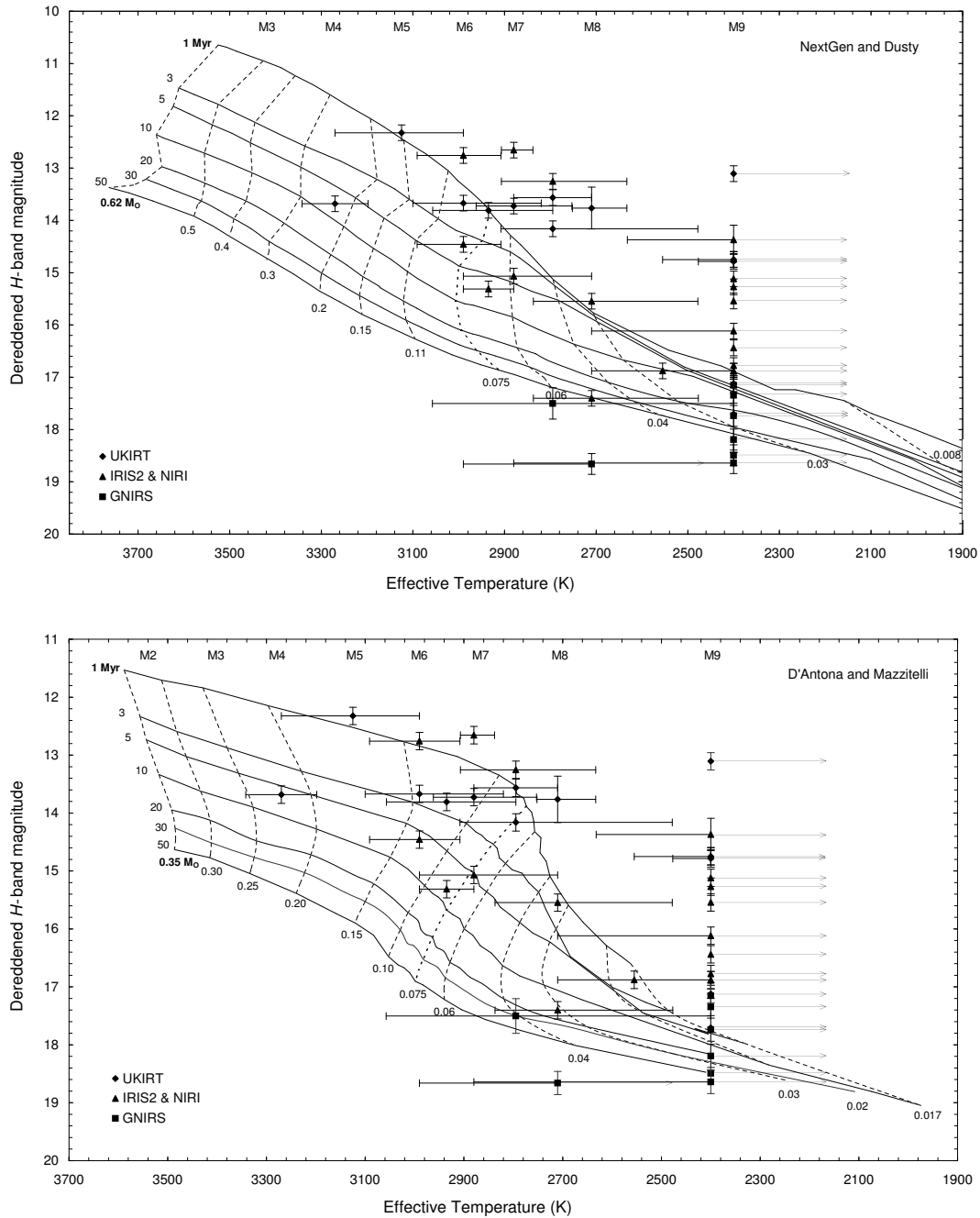
[1] http://www.astro.caltech.edu/~jmc/2mass/v3/transformations/

Figure 5. H-R Diagrams for the ONC are shown with the combined NextGen and Dusty isochrones of Baraffe et al. 1998; Chabrier et al. 2000 and Allard et al. 2001 (top), and the pre-main-sequence models of DM97 (bottom). Arrows represent upper limits for effective temperature.

burst of star-formation. Evidence of a broad and possibly bimodal age distribution was observed by SHC04. However, RRL do not see a dichotomy in the H-R diagram. It is uncertain whether the different positions of individual sources in the H-R diagram are really due to different ages. As discussed by Siess et al. (1999) and Tout et al. (1999), sources on the Hayashi track, still contracting and/or accreting, are subject to scatter on the H-R diagram. In the Hayashi re-

gion accretion generally leads to bluer colours which results in an overestimate of the age. The evolution of an accreting star is also accelerated which can cause it to appear older in the H-R diagram. For this reason the H-R diagrams for star-forming regions have significant scatter in comparison to those based on stable main-sequence stars. Briceño et al. (2002) and SHC04 suggest objects with optically thick disks observed virtually edge-on may be observed in scat-

tered light. The consequence of this is an underestimation in luminosity for a given effective temperature on the H-R diagram, resulting in objects that appear older than they really are. Due to the fact that a very small number of our objects lie close to the 10 Myr isochrone, this scenario may be a reasonable interpretation. The detection of objects in scattered light may provide an explanation for the location of two GNIRS objects (107-453 and 092-532) with effective temperatures > 2500K that appear to have ages ⩾30 Myr in each diagram, and NIRI source (030-524) that appears ∼50 Myr in age in the diagram that uses the NextGen and Dusty isochrones. Although the error bars are large for these objects, visual comparisons with the template spectra in the Luhman sample suggest that the spectral types have been constrained well. Under-estimation of source flux due to scattering is therefore another possible explanation for the abnormal location of these objects on the H-R diagram.

The H-R diagram is most interesting below 2500K. 12 sources are located a considerable distance above the 1 Myr isochrone in both plots. The reduction and spectral typing of these sources was thoroughly checked and photometric measurements taken at two different epochs (Lucas et al. 2000 using UFTI on UKIRT and Lucas et al. 2005 using Flamingos on Gemini South) were compared for differences. Significant changes in flux, attributed to source variability, were found for four objects in our sample. These were <0.3 magnitudes at H-band for two of the sources. The remaining two sources showed larger discrepancies of 0.5 and 1.16 magnitudes at H-band. For the photometrically discrepant objects H-band photometric data was used that was obtained at an epoch closest to the spectroscopic observation. The dereddened H-band error bars were increased in size for these objects to account for photometric scatter. The effect of variability in young stellar objects is most significant at K-band (Kaas, 1999). For the majority of our sample photometric uncertainties due to variability appear to be small (∼0.15 mags at H-band) and do not have a significant effect on our H-R diagrams.

The extreme scatter of some objects above the 1 Myr isochrones can not be explained by a population of unresolved binary sources. Even an unresolved system of three similar objects still only accounts for ∼1.2 magnitudes and cannot explain the excess flux of up to 3 magnitudes. The presence of unresolved systems is clearly an unsatisfactory interpretation of the unusual location of this group of objects. There is potential for a discrepancy in the assumed distance to Orion (450 pc). However, the likelihood of this being much greater than 50 pc is small based on the scatter present in many independent distance measurements (e.g. Walker (1969); Breger, Gehrz & Hackwell (1981); Stassun et al. (2004); Jeffries (2007)). If we assume Orion is situated at a closer proximity of 400 pc, the isochrones become marginally brighter, with a minor shift of ∼0.26 magnitudes. This shift makes an insignificant difference to the H-R Diagram. In order to bring these objects to the 1 Myr isochrone a minimal shift of 3 magnitudes is required in some cases. Such a large shift is unreasonable for several obvious reasons. Eg. it would require that most of the sources are ∼20-50 Myr old which would be inconsistent with the spectroscopic observations. It is unlikely that these objects are nearby foreground sources because the spectral profiles are indicative of young, low surface gravity objects.

A possible interpretation of these discrepant sources is that they represent an extremely young population of objects. The NextGen and Dusty models do not extend to ages below 1 Myr so a visual comparison to reliable model data is not possible. The DM97 models generate data that extend below the age of 1 Myr and can be used to give an indication of the physical properties of extremely young objects. Isochrones younger than 1 Myr have not been plotted in Figure 5 due to the fact that there is no calibration available from the NextGen and Dusty models. Levine et al.(2006) plot an H-R diagram for NGC 2024 (Orion B molecular cloud). This includes DM97 pre-main-sequence isochrones that extend to an age of 0.1 Myr. The data for the 0.1 Myr isochrone is limited to ∼2500K. At 2500K the isochrone is nearly vertical and fainter than the majority of the outlying objects in our sample. It therefore fails to explain the outlying sources that lie above the isochrone. The reliability of model isochrones tails off significantly at ages less than 1 Myr. This is partly to do with the fact that there is variability in the initial conditions. In addition to this the DM97 models are relatively imprecise compared to the NextGen and Dusty models. For these reasons we cannot rule out that the location of these objects in the H-R diagram is due to extreme youth. Furthermore the spectral types for these objects were calibrated from template spectra of objects 1-2 Myr in age. Like other authors (e.g. Levine et al. 2006) we have assumed that extremely young objects will have spectral profiles very similar to those a few Myr in age. However, if we are looking at a population of objects ≪1 Myr in age with very low surface gravities, the water absorption bands may be deeper than in objects with similar temperatures that are several million years older. This will lead to spectral types that are too late. With small age differences the extent of the effect is not likely to be large.

A possible interpretation of these bright objects is that they are spectrum variables. It is possible that the spectra of these objects are varying on relatively short timescales due to active accretion (see eg. Rodgers et al. 2002). Further near-infrared spectroscopic and photometric measurements are required to determine whether the spectra are varying over time.

A total of 17 sources from this sample have been observed spectroscopically at optical wavelengths by RRL. 9 of which are included in the UKIRT sample. The optical sample also includes 5 IRIS2 and 3 NIRI objects. 12 of the 17 sources that have been observed spectroscopically in both data sets agree to within 1 spectral subtype. A further two objects agree to within 1.25 subtypes. The remaining three objects have differences of 1.50, 2.25 and 2.75 subtypes. The two largest discrepancies are for the UKIRT objects 096-1943 and 055-230, respectively. This is particularly interesting as both of these sources appear late at near-infrared wavelengths (096-1943 = M9.0±0.5; 055-230 = M9.5±0.5). 096-1943 and 055-230 have optical spectral types of M6.75±0.5 and M6.75±1.5, respectively. The error bars for these two objects cannot account for the large discrepancy observed. 096-1943 and 055-230 are both cool objects that are significantly offset from the 1 Myr isochrone in the H-R diagram. The optical observations of these objects were obtained at different epochs to the infrared UKIRT data. This may be evidence for two spectrum variable objects. The difference is unlikely to be due to data quality as

the brightness of these sources ensured good data quality in the optical and infrared. The only other M9 to M9.5 object observed at optical wavelengths is 031-536. For this object RRL found an optical spectral type only 0.75 subtypes earlier than us. In addition to this 031-536 is much closer to the 1 Myr isochrone.

In all but 3 cases, our spectral types are slightly later than those derived at optical wavelengths. The observed offset is ⩽ 1 spectral sub-type, typically in the order of 0.5-0.75 sub-types. If the optical spectral types are more reliable then a significant number of our objects will move closer to the 1 Myr isochrone in the H-R diagram. However, the average cluster age will remain < 1 Myr. The H-R diagrams published by RRL & Peterson et al. 2008 are in very good agreement with ours, showing a distinct population of objects above the 1 Myr isochrone. Below 2500K RRL and Peterson et al. 2008 also see a population of bright sources that are significantly offset from the 1 Myr isochrone, thus confirming our results are not due to a systematic error.

We compare our spectroscopically determined temperatures to the photometrically derived temperatures determined from dereddened (I-J) colours and the 1 Myr NextGen isochrone (Figure 6). Some objects in our sample are not detected at I-band because they are too faint. These have been excluded from the plot. Sources covered at optical wavelengths by RRL are plotted as circles, extra sources from our sample are plotted as triangles. Sources with spectral types > M9.5 are marked as upper limits. The photometric and spectroscopic temperatures agree reasonably well despite some scatter in the results. In general the photometric measurements slightly underestimate effective temperature, typically by ∼100 K. The trend is similar to that seen by RRL. However, the spectroscopic temperatures derived at near-infrared wavelengths are significantly closer compared to the optical results of RRL. 4 sources in Figure 6 have photometric temperatures that are much hotter than measured from spectroscopic data. 3 of the 4 outlying sources are from our data alone and have anomalously blue (I-J) colours, as defined by Lucas & Roche (2000). This suggests that they have associated circumstellar matter and modified colours due to scattered light. The remaining source was also observed at optical wavelengths and has a derived spectroscopic temperature that is consistent with ours.

RRL found that optical sources with spectroscopic temperatures > 3200 K had photometrically derived temperatures that were much hotter. We only have one cluster member in our sample hotter than 3200 K (091-017). This source was also observed at optical wavelengths but calculated to be cooler than our spectrally derived value. The spectroscopically derived temperatures are probably more reliable than those derived from (I-J) photometry, in part because the spectral types are derived from more than one index. The I-band fluxes are more likely to be influenced by scattered light or even free-free emission from circumstellar matter (for sources located in the ONC HII region).

In Figure 7 we plot photometric mass against spectroscopic mass. Sources are identified by the same symbols used in Figure 6. Photometric masses are determined using the 1 Myr NextGen and Dusty isochrone together with the dereddened H-band magnitude for each source. Mass tracks are approximately vertical between isochrones of different ages on an H-R diagram (see Figure 5). This means that minor
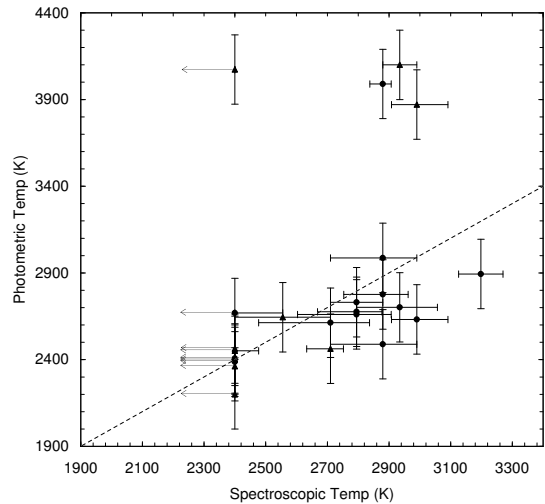

Figure 6. Comparison of photometric and spectroscopic temperature. Photometric temperatures are derived from dereddened (I-J) colours by comparison with the NextGen 1 Myr isochrone. Spectroscopic temperatures are from this work. Sources in our infrared sample covered by RRL at optical wavelengths are depicted by circles. Objects observed in our data set alone are displayed as triangles. Cluster members with spectral types >M9.5 are plotted as upper limits.

errors in assumed age that may exist will have a negligible impact on mass. Spectroscopic masses and their errors are taken directly from this work. The agreement between photometric mass and spectroscopic mass is reasonable if we exclude sources that are plotted as upper limits. However, when we include every source the overall agreement is poor. The results show significant scatter, with the majority of the sources having photometric masses that are higher than those derived from our spectra. The overall agreement between photometric and spectroscopic mass is better at optical wavelengths (see RRL), although significant scatter still exists. One source from our sample that is also covered in the optical sample of RRL (091-017) has a photometric mass that is significantly lower than our derived spectroscopic mass. The water absorption in the spectrum of this M4.5 source is weak in comparison to sources that have masses close to the hydrogen burning limit, demonstrating that photometric data alone was insufficient to accurately determine the mass. The outlying object is possibly surrounded by circumstellar material and subsequently observed in scattered light. Only 1 of the 4 significantly outlying sources (121-434) in Figure 6 shows a reasonably large difference between photometric and spectroscopic mass in Figure 7. 121-434 was observed at optical wavelengths by RRL. They derive a spectral type of M 5.5 for this object which differs from our derived value of M 7.0. The earlier spectral type gives better agreement with the photometric mass (0.1 $M_\odot$ difference). However, the spectroscopic temperature still differs from the photometric temperature by ∼900 K.

The comparisons made in Figures 6 and 7 demonstrate that we can not rely on photometric data alone to determine the physical properties of sources. SHC04 also observe inconsistencies between photometric and spectroscopic masses,
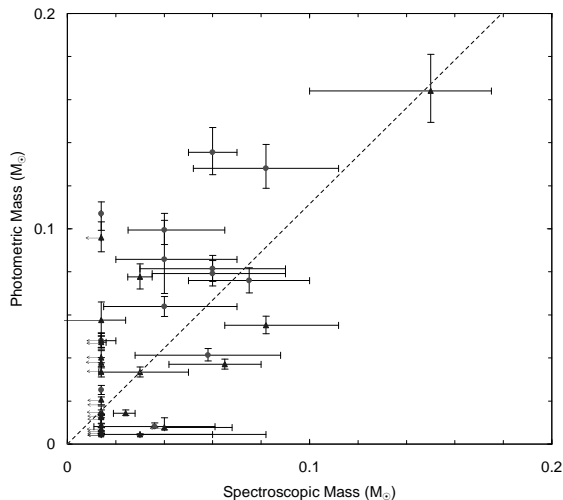
Figure 7. Comparison of photometric and spectroscopic mass. Photometric masses are calculated from dereddened H-band magnitude and the 1 Myr NextGen and Dusty isochrone. Sources in our infrared sample covered by RRL at optical wavelengths are depicted by circles. Objects observed in our data set alone are displayed as triangles. Cluster members with spectral types >M9.5 are plotted as upper limits.

and come to the same conclusion. We find photometric temperatures are more reliable than photometric masses.

5.2 Source Mass and Age of Cluster

Masses have been determined for the ONC sources using the NextGen and Dusty pre-main-sequence isochrones. Source masses were derived by interpolating between isochrones and mass tracks. For sources less than 1 Myr in age, masses were determined by lowering each object down to the 1 Myr isochrone. The effective temperature was kept constant in all cases. Due to the fact that the mass tracks are approximately vertical in the regions where this procedure was carried out, the approach is acceptable. The quoted errors in derived mass are based on the uncertainties in effective temperature and therefore do not take into account the uncertainty in the spectral type to effective temperature conversion.

Based on the pre-main-sequence NextGen and Dusty isochrones, 36 of the 40 sources plotted in the H-R diagrams lie below the hydrogen burning limit (0.075 $M_\odot$). The remaining sources are low mass stars. 17 of the 36 sources from this work have masses that are potentially below the deuterium burning limit (The status of these objects are discussed in more detail in Section 5.3). However, the template spectra must be extended to include cooler objects before we can calibrate these sources accurately. To account for this we assign these objects with a mass that is an upper limit (0.014 $M_\odot$). If we adopt the pre-main-sequence models of DM97 the number of sources that lie below the hydrogen burning limit declines from 36 to 29. Source masses are presented in Table 3.

We adopt an age of 20 Myr for the NIRI source 030-524 as it is unlikely to be 50 Myr in age. 3 GNIRS sources appear older than 10 Myr in age in both H-R diagrams. Two of these (016-430 & 092-532) have large errors in effective temperature which can account for their age discrepancy. The

remaining GNIRS source (107-453) could feasibly be greater than 10 Myr in age. Masses were determined for the GNIRS sources in paper 1. 3 more GNIRS sources have upper limits to their temperatures and so may shift to younger ages.

Comparison of the position of objects in the H-R diagram with the Lyon group isochrones suggests an average cluster age that is less than 1 Myr. We find no strong evidence that supports a significant population of mid M-type objects >10 Myr in age, but have excluded objects older than 50 Myr. This contrasts with results from SHC04, where a bifurcation of the H-R diagram can be seen in their data, for sources that were located in a more central region of the ONC. RRL have an H-R diagram that is in agreement with ours (and covers the same region of the ONC), showing few objects close to the 10 Myr isochrone and the majority above or close to the 1 Myr isochrone. A small bias may exist in the RRL data due to the fact that the fainter, older sources are difficult targets for optical spectroscopy, (although RRL showed that they would have detected a large population of 10 Myr sources.) However, the luminosity bias in our sample is no more severe than that in SHC04, so we should definitely see 10 Myr objects even if they are only a small fraction of the population.

Based on HST data, RRL provide evidence that showed 4 of the 14 apparently old sources (29%) in SHC04 are proplyds (see O'Dell & Wen 1994) and are therefore not old sources. It is possible that more of these apparently old objects are proplyd sources or young, embedded YSOs. However, inspection of the polarimetric dataset of Tamura et al.(2006) finds no evidence of unusually high polarisations, which might be expected if they had associated circumstellar matter. The objects in our sample were primarily selected from a location West of the brightest nebulosity. SHC04 obtained spectra of objects from the inner $5'.1 \times 5'.1$ of the ONC. The nature of the remainder of the apparently old objects detected by SHC04 therefore remains unclear.

5.3 Planetary mass Candidates

Formally calibrated template spectra do not exist for pre-main sequence sources later than M9.5. However, Lodieu et al. (2008) have provided spectral types ranging from M8-L2 for 21 brown dwarfs in the Upper Sco association, based on near infrared spectroscopy. In their work sources later than M9 were assigned pseudo spectral types based primarily on the spectral profile at J-band and the strength of the H_2O absorption in the H- and K-band. In the absence of other calibration spectra we have used the data of Lodieu et al.(2008) to derive spectral types for the 17 sources in this dataset that have derived types of M9.5 or later, by over-plotting and visually inspecting spectra from Lodieu et al.(2008). We note that the higher gravity expected for sources in Upper Sco, which has a mean age of ∼5 Myr, may cause us to derive types that are slightly too late, owing to the fact that the water absorption bands usually appear stronger in younger sources with low gravity. The results are presented in Table 4. The final spectral type (pseudo type) was determined from the average of the H and K types, if data in both bandpasses was available. All sources appear to have spectral types M9.5 or later. This finding agrees well with the spectral typing results presented in Table 3. 2 sources have spectral types of M9.5, 11 have types ranging from L0 to L1
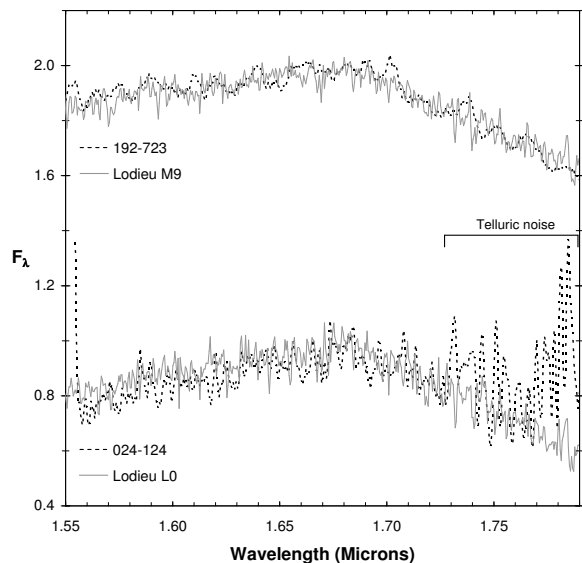
Figure 8. The spectra of an M9 and L0 object from Lodiue's sample over-plotted onto the *H*-band spectra of 192-723 and 024-124, respectively. Due to poor observing conditions and the relatively low altitude of the AAO, telluric noise is present beyond 1.72 μm in the spectrum of 024-124. The spectral profile of 192-723 clearly matches that of the M9 object. For 024-124, H_2O absorption sortward of 1.68 μm is consistent with that of an L0 source. Absorption longward if the peak is also consistent before telluric noise dominates the spectrum.

and 4 have a spectral type of L1.5. The *H*-band spectrum of 087-024 and *K*-band spectra of 084-104, 196-659, 188-658 and 152-717 have low S/N and therefore have pseudo types which are less robust. The reliability of this process can be seen in the *H*-band spectra of 192-723 and 024-124 in Figure C1.

    H-band magnitudes have been compared to the 1 Myr Dusty isochrone to determine whether these objects are likely planetary mass objects (PMOs). This was done for the GNIRS sources in paper 1, and so analysis has only been carried out on the remaining 12 objects. Sources that have dereddened *H*-band fluxes 0.5-0.75 magnitudes brighter than expected for a 13 M_J object with an age of 1 Myr ($H \simeq 17$ according to the Dusty isochrone) have been assigned the status 'uncertain' (see the final column of Table 4). Sources that are even brighter than this are marked as 'BD' which stands for brown dwarf. Sources that are fainter than expected for a 13 M_J object at 1 Myr, or within 0.5 magnitudes, of this value, are listed as PMOs. 4 of the 12 sources (024-124, 055-230, 061-400 and 084-104) are categorised as brown dwarfs and a further 3 sources (031-536, 056-141 and 192-723) have uncertain status. A total of 10 out of the sample of 17 PMO candidates are probable PMOs if they have ages of ∼1 Myr.

    In Appendix C we plot an H-R diagram that includes the spectral types that were derived using the template spectra of Lodieu et al. 2008. These replace the late type objects in our sample ($\geqslant$M9.5). Sources calibrated from the Lodieu spectra are marked as open triangles. The NextGen

Table 4. Pseudo spectral types for the 17 sources that appear to have spectral types M9.5 or later in Table 3.

ID	*H*-	*K*-	Pseudo Type	Prob. PMO[a]
015-319	low S/N	L1.5	L1.5	PMO
024-124	L0	——	L0	BD
031-536	L1	——	L1	Uncertain
037-628	L0	——	L0	PMO
055-230	L0	∼L0	L0	BD
056-141	L1/L2	——	L1.5	Uncertain
057-247	∼M9.5	∼L1	L0	PMO[c]
061-400	L1	——	L1	PMO
084-104	L1.5	L1?[b]	L1	PMO
087-024	L0[b]	——	L0	BD
130-053	∼M9.5	——	M9.5	BD
137-532	L2	L1	L1.5	PMO[c]
152-717	L0	L0?[b]	L0	PMO[c]
183-729	L0	L2	L1	PMO[c]
188-658	L0	L0/L1[b]	L0.5	Probable[c]
192-723	∼M9.0	L0.5	M9.5	Uncertain
196-659	——	L1/L2[b]	L1.5	PMO

notes:
[a] This estimate is based on *H*-band photometry.
[b] Spectral type may be erroneous due to low signal to noise in spectrum.
[c] PMO status derived in paper 1 (Lucas et al. 2006).

and Dusty isochrones have been used. Temperatures were estimated from field dwarfs using data from Martín et al. 1999. Due to the fact that these values are estimated an error of $\pm$150 K has been used. The H-R diagram provides a reasonable estimate of the positions of these late M / early L-type objects.

6   SURFACE GRAVITY AND CLUSTER MEMBERSHIP

The surface gravity of an object is an important parameter to constrain as it allows us to determine whether a particular source belongs to a cluster. The broad absorption bands seen at near-infrared wavelengths are good indicators of surface gravity (see Section 3). Surface gravity was ascertained by studying the spectral profile of each source. In addition to visual inspection a statistical test that makes comparisons to high and low gravity spectra was used. This was required because of the low signal to noise of the data. The statistical test is a useful back-up analysis for the *K*-band data, where the difference in spectral profile is more subtle. The same computational analysis was used to determine surface gravity in paper 1. For a description of how the code works see Lucas et al. 2006. Both visual inspection and computational results were used to estimate the gravity of each object. Analysis was not carried out on sources with a Rayleigh-Jeans type continuum. The surface gravity results are presented in Table 5. The table includes sources from Lucas et al. 2006.

    If the minimum χ^2 result agreed with the visual interpretation, an object was assigned a corresponding gravity status. No formal cut-off in the difference in minimum χ^2 was used to decide whether an object was most likely a high or low gravity object. Differences in minimum χ^2

that were greater than 2 were taken to be clear indicators of surface gravity. In all but 1 of the cases where a difference this large occurred (024-124), the nature of the surface gravity appeared to be obvious from the spectral profile. Limited wavelength coverage in the spectrum of 024-124 was the reason that surface gravity was uncertain from visual scrutiny. In cases where the difference in minimum χ^2 was less than 1, the gravity of an object was only given a gravity measurement if the visual interpretation matched the lower χ^2 result. For cases where the difference in minimum χ^2 was very small or did not agree with the visual interpretation the gravity status was labelled *uncertain* or *probably low* depending on the individual case. Candidates thought to have low surface gravity are assumed to be definite cluster members and are denoted *CM* in Table 5. Sources with uncertain gravity have been denoted *U*. All sources observed at optical wavelengths by RRL were shown to have very weak absorption of the Na I doublet at 8183/8195 Å. This feature is a clear indicator of low surface gravity and thus very strong evidence that the sources are very young and belong to the cluster. For this reason the objects in Table 5 that were observed at optical wavelengths have been classed as low surface-gravity objects and marked as confirmed cluster members. The membership status of 011-027 was found to be unclear by RRL. Due to the fact that the spectrum of this object shows a smoothly declining Rayleigh-Jeans tail we cannot determine whether or not this object is a cluster member and have therefore excluded it from Table 5. 31 sources have spectra that are more consistent with low-g late M or early L-type templates than high-g templates in the H- and/or K-bands. The low gravity status is also probable for 016-410, 087-024, 156-141 and 188-658. However, the evidence is less clear for these objects. The K-band fits are poor for 107-453. This seems to be due to an unusually high flux at $\lambda > 2.2$ µm. This could be due to circumstellar dust emission, which would suggest that it is indeed a very young objects and a bona fide cluster member. 016-430, 092-532, 044-527 and 013-306 each have minimum χ^2 values that are not significantly different for the high and low-g templates. The minimum χ^2 fit for 013-306 occurred for a high-g template, despite having a spectrum that appears to have low surface gravity upon visual inspection. The χ^2 results for 192-723 indicate that the spectrum is more consistent with a high gravity L dwarf than a low gravity field dwarf. Photometric measurements suggest that this source is too bright to be a 1 Myr PMO. A very young PMO at the distance of Orion is expected to be fainter than m_H=17.2. The apparent magnitude of 192-723 is m_H=16.08 and it has visual extinction A$_v \simeq$4.5. A background field dwarf with a spectral type $\geqslant$ M9.0 can also be ruled out based on photometric measurements. It is possible that this object is a foreground field dwarf. However, it is also possible that it is a low mass cluster member that is very young ($\ll$ 1 Myr in age). A final explanation for this result is that the template spectra for young objects do not extend to sufficiently late spectral types. The spectrum of 192-723 shows very strong water absorption which is stronger than that seen in any of Luhman's calibration sample. The lack of CO absorption in the K-band spectra also provides evidence that this may be a young object as CO is often seen to be stronger in absorption in late-type field dwarfs. A final observation that may suggest the object is a foreground brown dwarf is that the signal to noise

is very good in comparison to that seen in the other spectra that have late spectral types. The spectrum of 037-628 is very noisy and contains a lot of structure. For this reason it was not possible to achieve a low value of χ^2. This object is therefore classified as an uncertain cluster member.

Gorlova et al. 2003 provide evidence of gravity sensitivity of Na I at K-band (2.21µm). The molecular feature is shown to be weaker in absorption in young cluster objects compared to field dwarfs of the same spectral type. However, the Na I absorption feature can not yet be used to accurately measure surface gravity. A selection of high quality spectra is required to construct a reliable spectral type to surface gravity relation for the Na I feature at 2.21 µm. In general the K-band spectra are too noisy to accurately identify and measure the equivalent widths of the Na I feature. However, there is some evidence of the absorption feature in the spectra of 192-723, 010-109, 186-631, 091-017, 084-1939, 014-413, 096-1943, 013-306 and 095-058. Although these features cannot be used to derive definite gravity measurements, their apparent weakness provides further evidence that they are probable cluster members. Despite the indication of a weak Na I feature in the spectrum of 013-306, the overall gravity status is uncertain from visual interpretation and χ^2 comparison.

The χ^2 and visual analysis demonstrate that 33/40 of the low mass candidates are probable cluster members. The majority of uncertain cluster members in Table 5 have spectral types that are M8 or later. The expected number of M9-L5V solitary field dwarfs lying between Earth and Orion in the 26 arcmin^2 field of view of the deep Gemini imaging data from Lucas et al.(2005), is 0.36-0.72, down to H=19. This rises to 0.61-1.22 objects when unresolved binaries are included (Lucas et al, 2006). 21 sources in Table 5 have spectral types $\geqslant$ M9.0, 14 of which are in the field of view of the Gemini imaging. By assuming a Poisson distribution with a mean of 1.22 for field contaminants, it is possible to estimate the probability of different numbers of non cluster members being present in the 26 arcmin^2 area with $\geqslant$M9.0. With the above assumptions the likelihood of 7 or more sources being foreground field dwarf contaminants is 0.16%. The probabilities of >3 and >2 contaminants are 3.55% and 12.49% respectively. When M6 - M8 objects are included, the expected number of contaminating objects rises by a factor of $\sim$2 (Lucas et al. 2006). It is therefore feasible that a few of the sources which have an uncertain gravity status are foreground field dwarfs. Contamination is most likely for the sources with the earlier spectral types. Contamination by field dwarfs at the distance of Orion and/or behind the cluster can be ruled out. This is because the typical absolute magnitudes for M9 and L5 field dwarfs at K-band are 10.29 and 11.61, respectively (Kirkpatrick et al. 2000). The χ^2 fits rule out contamination from any objects later than L1.

7   MODELLING AGE AND MASS

The substellar IMF and age distribution for the ONC are still poorly constrained. This is because a very large number of high quality optical and infrared spectra are required to confirm cluster membership and fully characterise the population. One measurement that is well constrained for the ONC is the luminosity function. A Monte Carlo approach

Table 5. Gravity and cluster membership. Source-names of objects observed at optical wavelengths by RRL which have been shown to have low surface gravity from measurements of the Na I doublet at 8183/8195 Å are in italics. The table includes sources from Lucas et al. 2006. Sources with low surface gravity are marked as cluster members CM. Objects with uncertain gravity status are not definite cluster members and are denoted by U. Probable cluster members are denoted CM?. The spectrum of 037-628 contained too much structure for a reliable fit to be determined. Objects spectral typed ⩾9.5 are below the dotted line.

Source	Type	Visual (g)	Spectral Type : minimum χ^2 low-g H-	high-g H-	low-g K-	high-g K-	Gravity	Status
091-017	M4.5	Low	M4.5: 1.66	M7.0: 2.08	M5.5: 2.54	M6.0: 2.66	Low	CM
016-410	M5.0	Uncertain	M4.5: 3.07	M4.0: 3.19	—-	—-	Prob. Low	CM?
067-651	M6.0	Uncertain	M5.5: 15.1	L1.0: 16.9	—-	—-	Low	CM
069-209	M6.0	Low	M5.5: 2.37	M8.0: 3.63	—-	—-	Low	CM
077-453	M6.0	Low	M5.5: 10.6	M8.0: 14.7	—-	—-	Low	CM
019-354	M6.5	Low	M6.5: 2.26	M9.0: 2.29	M6.5: 2.86	M8.0: 3.08	Low	CM
255-512	M6.5	Low	M5.5: 7.34	M8.0: 10.7	—-	—-	Low	CM
068-019	M7.0	Low	M5.5: 1.25	M8.0: 1.70	M6.5: 1.72	M8.0: 2.54	Low	CM
121-434	M7.0	Low	M5.5: 9.50	M8.0: 14.1	—-	—-	Low	CM
186-631	M7.0	Low	M6.0: 3.29	M9.0: 5.95	M9.5: 6.99	M9.0: 20.1	Low	CM
014-413	M7.5	Low	M8.5: 2.89	L1.0: 2.92	M9.5: 2.56	M9.0: 4.89	Low	CM
053-503	M7.5	Low	M7.5: 2.25	L1.0: 2.01	M7.5: 2.42	M8.0: 9.91	Low	CM
092-532	M7.5	Uncertain	M6.0: 2.90	M7.0: 3.34	M6.0: 2.90	M7.0: 3.20	Uncertain	U
095-058	M7.5	Low	—-	—-	M9.5: 12.7	L1.0: 59.9	Low	CM
010-109	M8.0	Low	—-	—-	M7.5: 2.97	M8.0: 5.48	Low	CM
030-524	M8.0	Uncertain	—-	—-	M4.5: 3.01	M4.0: 3.13	Low	CM
043-014	M8.0	Low	M8.5: 2.03	M3.0: 2.99			Low	CM
107-453	M8.0	Uncertain	M9.0: 4.10	L1.0: 3.80	M9.0: 14.3	L0.0: 32.1	Uncertain	U
044-527	M8.5	Uncertain	—-	—-	M4.5: 3.60	M4.0: 3.76	Uncertain	U
013-306	M9.0	Low	—-	—-	M6.5: 5.20	M8.0: 4.62	Uncertain	U
016-430	M9.0	Uncertain	M9.0: 2.90	L3.0: 2.90	M9.0: 4.30	L1.0: 4.20	Uncertain	U
084-1939	M9.0	Low	M9.5: 3.03	L1.0: 6.83	M8.5: 2.40	M8.0: 6.13	Low	CM
096-1943	M9.0	Low	M9.0: 6.28	L1.0: 6.25	M9.5: 3.71	L1.0: 15.8	Low	CM
031-536	M9.5	Uncertain	M9.5: 2.25	L3.0: 2.32	—-	—-	Low	CM
055-230	M9.5	Low	M9.0: 4.19	L1.0: 6.16	M7.5: 4.21	M8.0: 4.99	Low	CM
087-024	M9.5	Uncertain	M9.0: 7.82	L1.0: 8.38	—-	—-	Prob. Low	CM?
057-247	⩾M9.5	Low	M9.0: 2.00	L1.0: 3.20	M8.0: 1.90	M9.0: 3.10	Low	CM
183-729	⩾M9.5	Low	M8.0: 2.90	L1.0: 3.20	M8.0: 3.70	M9.0: 5.70	Low	CM
015-319	>M9.5	Low	—-	—-	M9.0: 13.9	L1.0: 11.2	Uncertain	CM?
024-124	>M9.5	Uncertain	M9.5: 10.5	L1.0: 13.0	—-	—-	Low	CM
037-628	>M9.5	Uncertain	N/A	N/A	—-	—-	Uncertain	U
056-141	>M9.5	Low	M9.5: 7.84	L3.0: 12.7	—-	—-	Low	CM
061-400	>M9.5	Low	M9.0: 1.42	M3.0: 1.53	—-	—-	Low	CM
084-104	>M9.5	Low	M9.5: 1.52	M3.0: 1.53	M9.5: 18.2	L1.0: 22.0	Low	CM
130-053	>M9.5	Uncertain	M9.5: 56.3	L1.0: 82.6	—-	—-	Low	CM
137-532	>M9.5	Low	M9.0: 1.50	L2.0: 1.60	M9.0: 5.00	L0.0: 9.80	Low	CM
152-717	>M9.5	Low	M9.0: 2.00	L3.0: 3.20	M9.0: 5.70	L0.0: 8.70	Low	CM
188-658	>M9.5	Uncertain	M8.0: 5.90	L1.0: 6.70	M9.0: 4.40	L0.0: 5.20	Prob. Low	CM?
192-723	>M9.5	Low	M7.5: 25.3	L1.0: 23.2	M9.0: 13.2	L1.0: 6.35	Uncertain	U
196-659	>M9.5	Low	—-	—-	M9.5: 6.16	L1.0: 6.45	Low	CM

can be used to experiment with different age distributions and a variety of different mass functions, to generate a range of luminosity functions. The luminosity functions produced by different models can be compared to the real (deredened) luminosity function and tell us which initial conditions are most likely and unlikely. We created a program that allowed us to do this for the ONC. An explanation of how the program works and the parameters that were varied are described in Section 7.1. The results from the Monte Carlo simulations are described and analysed in Section 7.2.

A limitation of this approach is that we use the Lyon Group models to generate a luminosity function. The scat-

ter in the H-R diagram (see plot in Appendix C) shows that these models cannot fully describe what we observe. For example 055-230 (the source furthest from the 1 Myr isochrone) in Figure 5 is much cooler than predicted by the Lyon Group models. However, the temperatures of some of the brighter, outlying objects are uncertain (see Section 5.1) since two of them have earlier optical spectral types that are more consistent with the Lyon Group models. E.g. 055-230 has an optical type of M6.75 and an infrared type of M9.5 or L0 (the latter is the pseudo type which was calibrated from the template spectra of the Lodieu et al. (2008)). We do not think that this scatter will significantly affect the re-

sults of these simulations because the proportion of outliers is small. Also the spread extends to both warmer and cooler effective temperatures, which tends to cancel any inaccuracy or limitations of the theoretical models.

7.1   Model

In this section we give an overview of what the model does then go into detail regarding the parameters that can be varied.

Our model generates a luminosity function in the following way. A random number is scaled to generate an age based on a desired age distribution. A second random number is then used to generate a mass which is based on the type of mass function that has been chosen. The age and mass values are then used to select a pre-main-sequence isochrone of the derived age, and an *H*-band luminosity corresponding to the mass that was generated. The H-band luminosity value is then added to two[2] differently binned histograms. This is carried out for the same number of objects in our extinction limited sample of sources (explained in Section 7.2). This was done for convenience when normalising the histogram. The algorithm is repeated a million times. Finally the two histograms are normalised producing a luminosity function that is represented in a variety of bin sizes.

The model allows us to experiment with four types of age distribution. Variations can be made to two of the scenarios to give a total of six different types of age distribution. In all cases the earliest age that can be generated is 0.3 Myr, a limit chosen because younger sources are likely to be too deeply embedded in their natal cloud core to be present in our extinction-limited luminosity function. The most simplistic age distribution we use is flat. This scales a random number so that it has an equal chance of lying anywhere between 0.3 Myr and a maximum age prescribed by the user. The second type of distribution that can be selected is Gaussian. In this type of scenario the user can define the mean age and the standard deviation or spread. The third type of age distribution is skewed. We use a Gumbel Skew for this age function. The skew can be set to be positive or negative and also gives the user the flexibility of setting the mean age and the spread. The advantage of a skewed distribution is that it can simulate a sharp burst of star formation that declines over a period of time (-ve skew). Equally it is possible to investigate a scenario where the star-formation rate increases before dropping off more rapidly (+ve skew). The final type of age distribution that we investigate is bimodal. We chose to generate bimodal age distributions using two different methods, each of which was modelled in our simulations. The first was to use two Gaussians and the second to use two skews. In the case of two skews we decided the most realistic scenario was to use two -ve skews to simulate two bursts of star-formation that tail off over time. In the bimodal models the user was able to set the ratio of sources to be generated in each distribution.

The nature of the mass function could be varied in three different ways. By default a log-normal mass function as derived by Miller and Scalo (1979) was used. The mean and standard deviation of this function could be altered. We explored a further option that enabled the mass function to be altered by truncating the Miller and Scalo mass function by a user-defined power law at low masses. This enabled us to experiment with previously published values of α that have been used to describe the behaviour of the mass function as it extends down to the planetary mass regime. The final parameter allowed us to truncate the mass function at the deuterium burning limit. The reason for doing this was to see whether a population of planetary mass objects was required to produce a luminosity function that represented that observed for the ONC. We use a rejection algorithm to ensure that objects more massive than 1.2 M$_\odot$ are not created by the mass function since this is the upper mass limit of the NextGen model grid.

From the simulations a luminosity function that is based on the NextGen and Dusty pre-main-sequence models or those created by DM97 could be generated. However, only the NextGen and Dusty models were simulated. This is because the DM97 models do not extend below the deuterium burning limit, and that these models are thought to be less accurate. A limitation with our model is that the NextGen and Dusty isochrones do not extend to ages less than 1 Myr. For generated ages < 1 Myr we adopt luminosities from the 1 Myr isochrone. To some extent this will lead to a luminosity function that lacks objects at the brightest luminosities. However, based on our input parameters we do not believe that this will have a significant effect on the results. We tested this by creating a 0.5 Myr isochrone based on data from the DM97 models. Although this isochrone cannot be used for the final modelling results and analysis, it allows us to see what happens to the luminosity function when younger, brighter sources are added. The results revealed an interesting difference. In general there was a slight increase in the number of objects in the brightest bins, slightly reducing the number of objects in the faintest bins. The overall reduced χ^2 values improved by approximately 0.4 in the best fitting cases. This demonstrates that using a 1 Myr isochrone for sources younger than 0.75 Myr in age has a noticeable effect on the brightest and faintest end of the luminosity function. However, the overall change is subtle and doesn't alter the best fitting age and mass parameters. As previously mentioned, the 0.5 Myr isochrone is only an estimate so we cannot trust that the output luminosity function is reliable.

The histograms that represent the luminosity function are binned so that two use full magnitude bins and two use half magnitude bins. The two histograms that have complete magnitude bins are offset by half a magnitude. The two histograms containing half magnitude bins are offset by quarter of a magnitude. These different binnings were used in order to assess the effect of random statistical fluctuations that may be present in the observed luminosity function.

7.2   Calculation of χ^2

In order to make a comparison to our model luminosity functions we need to be sure that our observed luminosity function suffers no contamination and is complete at all magnitudes. To do this we use an extinction limited sample, including all sources with A$_V$ < 5. We use deep photometric data

---

[2] The code generates a further 2 histograms that have smaller bins. These have not been included in the paper due to the low number statistics.

from Lucas, Roche and Tamura (2005) to generate our observed luminosity function and converted it to a dereddened luminosity function using the Rieke & Lebofsky (1985) extinction law. Completeness limits were found for the faintest magnitude bins using the ADDSTAR routine in IRAF. By randomly generating faint sources throughout the field, the number of these detected in each magnitude bin was able to be determined. Contamination due to foreground and background stars and dwarfs is likely to be small. However, we expect contamination from background stars to exist in our sample. This will be most significant at the faintest magnitudes. We determine the contamination in each bin based on sources we believe to be background stars from our entire spectroscopic sample and an optical data set from RRL. Due to the relatively low number statistics we see no contamination in several bins. We fitted a low order polynomial across several bins to better determine the contamination where this was the case. We note that the contamination rate is consistent with a Besançon model calculation (Robin et al. 2003) which we used to calculate the number of sources ranging from M0-∼M6 out to 450pc over the same area of sky covered by our observations. The calculation predicts 9 sources in total but becomes incomplete at $H=19$ where we measure greater contamination. However, we are likely to include reddened background stars in our spectroscopic sample. The Beasançon calculation apparently predicts a larger number of foreground sources than the modified Wainscoat calculation shown in Hillenbrand & Carpenter (2000). In Figure 9 we present the corrected luminosity function as 2 alternatively binned histograms. In both histograms the final three bins were combined into one large bin to avoid very low number statistics. The final bin is therefore representative of 3 bins. The error on each bin was calculated using standard error propagation formula. The total error takes into account the Poisson error relating to the total number of sources observed in the bin, the error in the completeness correction and the error associated with the contamination correction. The completeness errors were calculated from statistics gathered when using the ADDSTAR routine. The dichotomy between cluster membership and contamination in each bin was represented as a binomial probability distribution. the fractional uncertainty was therefore calculated using the formula presented in Equation 10

$$\frac{\sqrt{npq}}{n} \tag{10}$$

Rather than freely explore a very large parameter space we chose to design a model grid that tested parameters that were close to those expected in Orion in order to reduce computational time. We made sure that parameters in our simulations deviated sufficiently from the most likely parameters to test whether the luminosity function changed significantly with less likely initial conditions. In total 296 different scenarios were tested.

We calculated a reduced χ^2 value for each scenario to determine which parameters approximate the luminosity function best. We calculate our degrees of freedom in each scenario as the number of bins being fit minus the number of free-parameters in the model. Despite the fact that the bimodal scenarios have more degrees of freedom, reducing the χ^2 did not change the luminosity functions with the lowest χ^2 quantity.

7.3 Model Results

Our best model fits have a reduced χ^2 somewhat in excess of unity. This is because the models cannot recreate the sudden drop in source numbers in the observed luminosity function close to $H=13.5$. The steep drop observed in the dereddened luminosity function may simply be a statistical fluctuation due to the small size of our extinction limited sample. It is not seen in larger, shallower surveys of the ONC (see below). All of the remaining bins can be well fitted by our models. Our lowest reduced χ^2 value is ∼5.1. (This value decreases to 3.3 when half-magnitude bin sizes are used. As previously mentioned histograms with smaller bin sizes are not included due to the low number of objects in each bin, which causes the χ^2 method to become invalid.) We do not expect to be able to perfectly recreate the luminosity function with the relatively basic IMF and age distributions used in our model. The low number of sources (<200) in the extinction limited sample mean that even if we had the age distribution and IMF correct we would not necessarily see a low χ^2. In fact we would require a significantly larger number of observed objects to represent the age population and IMF distributions. The importance of this modelling is to see which type of initial conditions are most likely in the ONC and which can definitely be ruled out.

The best fit to the luminosity function, based on the scenarios we experiment with, is a single negatively skewed age distribution. The skew has a low age spread and is centred at 1 Myr. The mass distribution is a Miller & Scalo IMF that peaks at 0.15 $M_\odot$ and is truncated by a power law in the form of $N(M)\alpha M^\alpha$, where $\alpha=+0.60$ (or -0.60 for those who prefer the alternative definition of α). In this scenario we do not truncate the IMF at the deuterium burning limit (0.012$M_\odot$). Using the same set of parameters with an $\alpha=0.31$ (based on the result of Lucas et al.2005) also gives reduced χ^2 values that are similar. The histograms for the two best fitting scenarios are plotted in Figure 11. α takes a value of 0.60 in the top four histograms and 0.31 in the remaining four. The 0.31 power law predicts the number of fainter sources better, whereas the 0.60 power-law recreates the brighter sources better. It is unsurprising that the single Gaussian and single positive skew scenarios also generate relatively good fits with these parameters as the age distributions give similar results with low age dispersions.

7.3.1 Requirements for Low Mass Objects

The most significant result from our simulations is that very few scenarios generate good fits to the luminosity function if we truncate the mass function at the deuterium burning limit ($< 0.012 M_\odot$). None of the best fitting scenarios have a truncated mass function. After the top eight best fitting scenarios for each type of luminosity binning, several truncated mass functions are ranked in the reduced χ^2 results. However, these occur infrequently. The scenarios that have a truncated mass function and are ranked in the top 28 best fitting models have no sources in magnitude bins fainter than $H=17.5$. Due to the fact that we have near-infrared spectra of very low mass objects in this magnitude range (this work and Lucas et al. 2006), the likelihood of these model scenarios being plausible is low. These results are ranked relatively high due to the relatively large uncertainty in the faintest
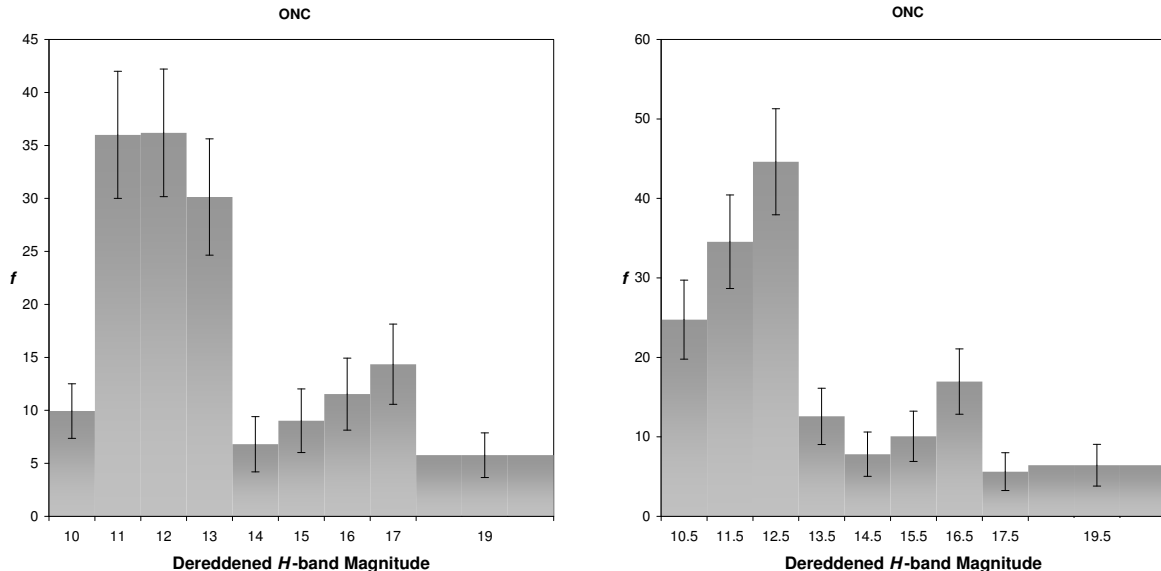
Figure 9. The measured extinction limited ($A_v < 5$), dereddened H-band luminosity function for the ONC. Two different binning variations are presented. The broad final bin in each of the diagrams was obtained by averaging three single magnitude bins that had low number statistics.

bins of the observed data. The brightest luminosity bins have more weight when calculating reduced χ^2 values. This means that model parameters that predict the number of sources in the brightest bins to a high standard will result in reasonable fits, despite having no sources in the faintest bins. The result would be clearer if we could recreate the luminosity function accurately at intermediate magnitudes. It is possible that the dearth of sources at H=13.5 in the observed luminosity function is a statistical fluctuation. Muench et al. 2002 observe a significantly larger sample ($\sim$1000 sources). The H-band luminosity function in their work shows a relatively smooth decline from H=12 to H=18, with a slight drop of in the number of sources between H=13 to H=15. However, reddening corrections have not been applied to the data.

The requirement for planetary mass candidates to recreate the mass function is perhaps most important in the scenarios that used a bimodal age distribution. Before running the models we anticipated that bimodal simulations, where $\sim 2/3$ of the sources are 1 Myr in age and $\sim 1/3$ belong to a population of sources $\geqslant$ 10 Myr in age, would create a bimodal luminosity function. However, this was not the case regardless of how we altered the mass function. We found that too few sources appear in the brightest bins when we sufficiently populate the faint bins. In addition to this the peak of the luminosity function moves towards fainter sources, producing a very poor fit. For every scenario, we experimented by truncating the IMF at the deuterium burning limit. In all nearly all cases this produced a worse result. We can therefore say with some confidence that a population of planetary mass candidates is required to reproduce the dereddened luminosity function in the ONC. Figure 10 shows 4 identically binned histograms of four different scenarios we ran. In each case the IMF was truncated at the deuterium burning limit. Further details on the model parameters are shown in the figure caption. The published re-

sults of planetary mass candidates in Orion, in paper 1 complement this result. We did not seriously investigate age distributions older than 10 Myr. This is because observational constraints tell us that very few ONC sources are >10 Myr in age. It is likely that we could recreate the luminosity function by truncating the mass function if we have a bimodal age distribution that has a population of objects 15-20 Myr in age. The bulk of sources in a simulation like this would need to be 1 Myr in age in order to sufficiently populate the brightest bins. We do not test such a scenario due to the fact that it is very unlikely, according to all published H-R diagrams for the ONC.

7.3.2   Age Distributions

As one may expect, a uniform age distribution is not ideal and struggles to recreate the luminosity function well, with no reduced χ^2 value being better than 11.9 for both types of luminosity binning. The best fit to the luminosity function when using a uniform age distribution has similar IMF parameters described above for the overall best fit (Miller & Scalo IMF truncated by a power law with an α of 0.60). The Monte Carlo simulations show that the above IMF parameters produce the best fit for each type of age distribution. The only parameter that varies in the best fit is α, which takes values of 0.31 and 0.60.

In general the bimodal scenarios produce the poorest fitting luminosity functions. We find that a bimodal age distribution is only suitable in the case where the ratio of 1 to 10 Myr objects is 10:1. In addition to this the spread of each age distribution has to be small (typically $\sigma \leqslant$1 Myr). If the fraction of 10 Myr sources becomes much larger, too few bright objects are created. Similarly if we make the spread of the bimodal Gaussians or Skews too broad (3-5 Myr), the sources are redistributed so that intermediate luminosity bins become most populated. The difference between cases
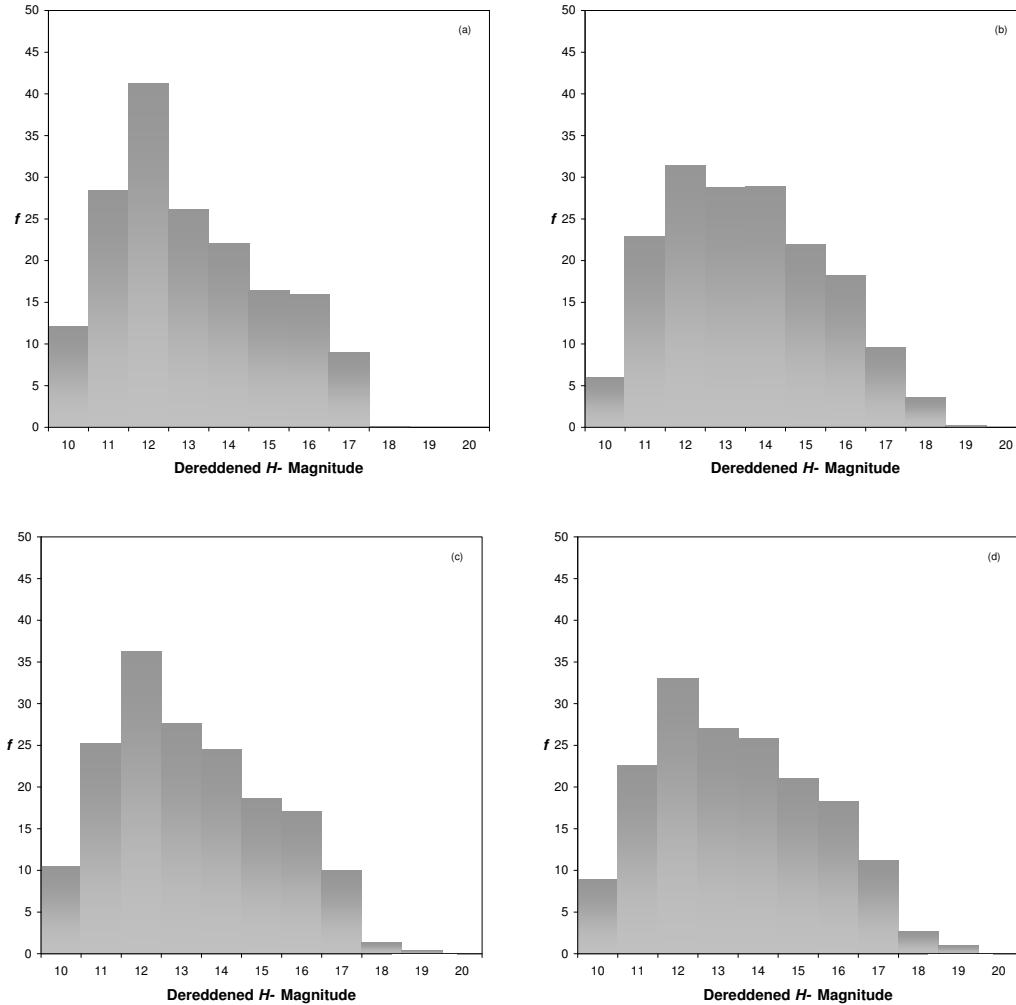
Figure 10. The effect of truncating the IMF at 0.012 M$_\odot$. The IMF parameters are the same for each of the synthetic luminosity functions displayed (Miller & Scalo above 0.15 M$_\odot$ and a declining power law with $\alpha = 0.31$ at 0.012-0.15 M$_\odot$.) Histogram (a) is derived from a negatively skewed 1 Myr age population with a 1σ age spread. Histogram (b) is derived from a Gaussian age population centered at 1 Myr, with a 3σ age spread. Histogram (c) is derived from a bimodal Gaussian age population centered at 1 and 10 Myr, with a respective ratio of 10 : 1 sources. Histogram (d) is derived from a bimodal Gaussian age population centered at 1 and 10 Myr, with a respective ratio of 3.3 : 1 sources. The Gaussians used for (c) and (d) had a 1σ age spread. In all cases the faintest H-band magnitude bins are starved of sources. To highlight this effect the faintest magnitude bins have not been rebinned.

running bimodal Gaussians and bimodal Skews is moderate. We find that negatively skewed bimodal age distributions generate better fitting luminosity functions than bimodal Gaussian distributions. We struggle to recreate the twin peaked luminosity function observed using a bimodal age distribution. Even with unrealistic extreme cases using 1 and 50 Myr age populations combined with a mass function that is truncated with a steep power law, we fail to generate a luminosity function with two clearly defined peaks. In bimodal scenarios where the ratio of 1 to 10 Myr objects was 1 : 0.7, the peak of the mass function was moved to $\sim 0.25 M_\odot$. This change in the mass function was made to try and ensure the brightest luminosity bins were sufficiently filled. This failed to work giving reduced χ^2 values of ~ 16. Instead the intermediate magnitude bins H=12.5-15.5 were over populated.

We analysed the results for single Gaussian and skew

populations and found that negatively skewed age distributions produce higher quality fits than Gaussian age distributions. The worst of the three was a positive skew. The results are consistent with those utilising bimodal age distributions. We find that single age distributions work well, providing a mean age of 1 Myr is used and the age spread is small. If the age spread is increased beyond a few Myr the peak of the luminosity function migrates from the brightest bins towards bins of intermediate magnitude, suggesting the age dispersion in the ONC is small. Our modelling results indicate that the star formation rate in the ONC has not been steadily increasing since an age of 10 Myr. As previously mentioned, a single negative skew produced the best overall fit to the observed luminosity function.

We summarise the results of the Monte Carlo simulations in Table 6. Rather than tabulate all the results we take the top three reduced χ^2 values for the single magni-
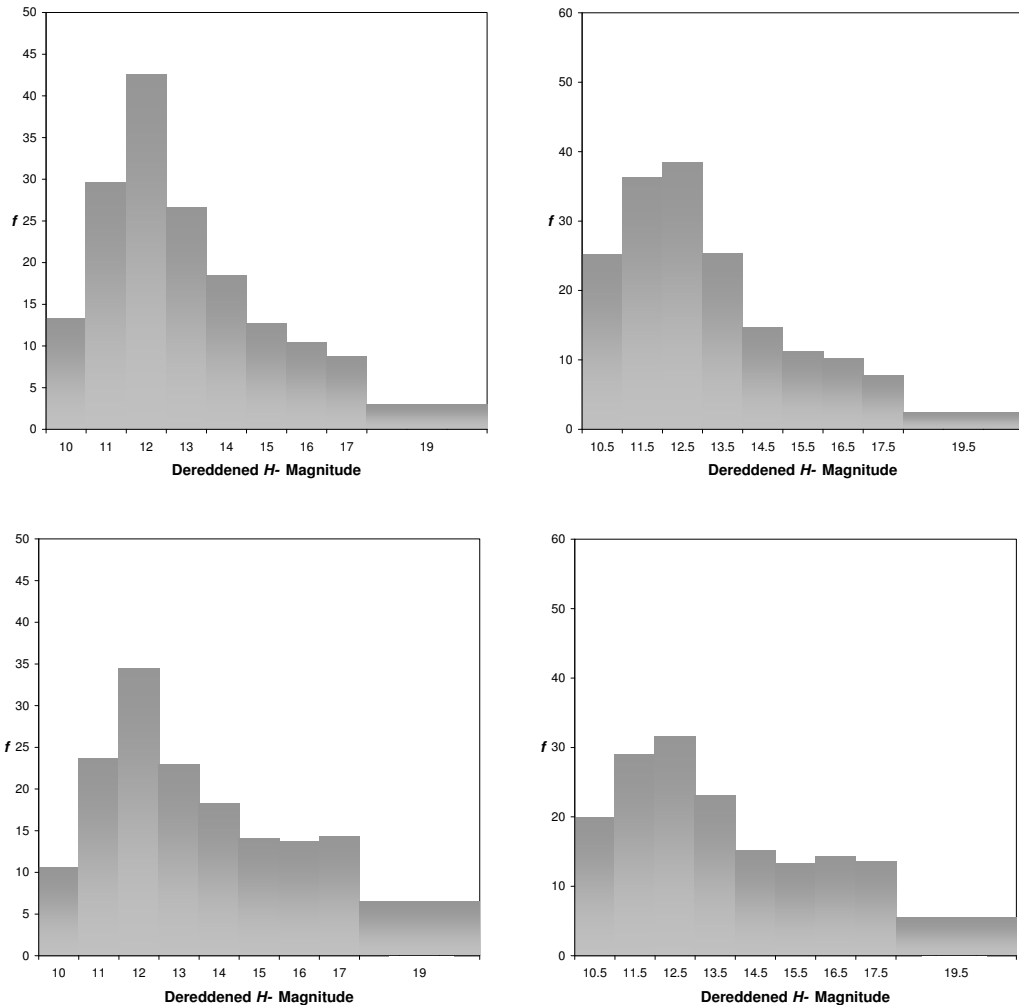
Figure 11. The luminosity functions for the two best fitting scenarios. Both are negatively skewed age distributions with a 1σ age spread and centred at 1 Myr. The mass distribution is a Miller & Scalo IMF that peaks at 0.15 $M_{\odot}$ and is truncated by a power law in the form of $N(M)\alpha M^{\alpha}$. α=0.60 in the top two plots and 0.31 in the remainder. In each case we fail recreate the sudden drop in sources that have luminosities ranging from $\sim 13 - 14.5$. χ^2 values are similar for both values of α. The low mass end of the luminosity function is best represented when α=0.31.

tude binned histogram. These histograms were offset by 0.5 magnitudes as shown in the right-hand image in Figure 9. Table 6 summarises how effective each type of age distribution is. In some cases lower reduced χ^2 values exist for different types of luminosity binning. However, in general the order of best fitting scenarios is essentially the same for both types of luminosity binning.

The star forming environment of the ONC is complicated and our Monte Carlo simulations have initial conditions that are somewhat simplistic. Therefore we cannot confidently suggest one particular formation history and IMF from our results. However, we can demonstrate which scenarios produce the best and worst fitting luminosity functions. Although the best fit to the luminosity function comes from a single 1 Myr age distribution (see Figure 11), the best fitting bimodal scenario (80% of the population having a mean age of 1 Myr and 20% of the population aged near 10 Myr. Miller-Scalo mass function with power law where α=0.31 and no truncation) generates a luminosity function

that is only subtly different. We know that 10 Myr objects do exist in Orion (e.g. Palla et al. 2005; Palla et al. 2007). The result from the negatively skewed 1 Myr age distribution provides evidence that the dominant age in the ONC is very young.

We have shown that the dominant age of objects in the ONC are likely to be $\leqslant 1$ Myr, and that objects older than this can exist providing there are not many. This result is consistent with what we see in our H-R diagrams and from the Li studies by Palla et al. (2005 & 2007). A broad age spread has detrimental effects on the luminosity function moving the peak to intermediate mass bins. This explains why a negatively skewed age populations, that include fewer old sources, always give lower reduced χ^2 values. Poor reduced χ^2 values for a 3σ negatively skewed age distribution appears to rule out an age distribution that has been continually rising since 10 Myr. However, our skewness is fixed. We expect a 3σ age distribution that is skewed more negatively will work better, producing fewer 5-10 Myr objects.

Table 6. Top three reduced χ^2 values for each type of age distribution. Results are derived from a histogram with a bin size of 1 magnitude, using the offset binning shown in the right-hand histogram of Figure 9. The results indicate a clear preference for a narrow age distribution centred near 1 Myr and an IMF that declines with decreasing mass in the brown dwarf regime.

Age Distribution	Reduced χ^2	Mean Age (Myr)	Age Dispersion (σ/Myr)	α	Truncated Mass Function?
-ve Skew	5.165	1	1	0.6	n
	5.728	1	1	0.31	n
	6.421	1	1	0.9	n
Gaussian	6.180	1	1	0.6	n
	6.560	1	1	0.31	n
	8.192	1	1	0.9	n
+ve Skew	9.329	1	1	0.6	n
	10.284	1	1	0.9	n
	10.403	1	1	0.31	n
Uniform	11.884	0.3-10	——	0.6	n
	12.598	0.3-10	——	0.31	n
	13.070	0.3-10	——	0.6	y
Bimodal (-ve Skew)	16.715	1 & 10 (10:1)	1	0.6	n
	18.568	1 & 10 (10:1)	1	0.9	n
	18.644	1 & 10 (8:1)	1	1.2	n
Bimodal (Gaussian)	20.149	1 & 10 (10:1)	1	0.6	n
	21.950	1 & 10 (10:1)	1	0.9	n
	23.774	1 & 10 (10:1)	1	0.31	n

We therefore deduce from our results that a continually rising star formation rate is only plausible if it is very low until $\sim$3 Myr. Age distributions >1 Myr produce poor results together with a uniform age distribution.

7.3.3 IMF

For all of the tested age distributions we found that the best associated mass function was that of Miller & Scalo (1979), truncated at $\sim$0.15 $M_\odot$ by an M$^\alpha$ power law with α taking a value of 0.31 or 0.60. The power represents low mass sources extending towards the deuterium burning limit. This is in agreement with measurements made by Lucas et al. 2005. Adopting α<0.3 over-populates the faintest bins and subsequently leads to poor χ^2 values. This remains true if the IMF is truncated at the deuterium burning limit. We tested the significance of altering the dispersion of the IMF. We found that increasing the dispersion added more high mass sources and removed faint sources. Decreasing the dispersion had the opposite effect. We find that the default dispersion prescribed by Miller & Scalo 1979 works best in the scenarios we test. Most importantly we find that altering this parameter does not help us remove sources from intermediate bins, where we struggle to reproduce the observed luminosity function. In most cases we find altering the mean and spread of the mass function from the best fitting values described above gives poorer results. In the vast majority of the scenarios that were tested, we require the mass function to extend to planetary masses to sufficiently populate the faintest bins. This is our most significant result.

7.4 Binarity

The modelling fails to take into account unresolved binary sources. Depending on the mass-binarity relation the overall profile of the luminosity function will change. Photometric measurements in the Pleiades and Praesepe regions by Pinfield et al. 2003 suggest the binary fraction increases as source mass decreases. This result is consistent with later work in the Pleiades by Lodieu et al. 2007. Their results suggests a binary fraction of $\sim$30-45% in 0.075-0.030 $M_\odot$ mass range. Estimates by Pinfield et al. 2003 and Lodieu at al. 2007 support the hypothesis that the brown dwarf binary systems are near equal-mass ratio systems. The mass range of 0.075-0.030 $M_\odot$ correlates to a range of H-band mags of 13.834-15.770 based on the Dusty and NextGen models. Assuming the most extreme case where all sources have identical mass and luminosity, cluster members that are part of an unresolved binary system will be 0.75 magnitudes brighter. Assuming the binary fraction remains constant below 0.030 $M_\odot$ and remains close to 30% for masses greater than 0.075 $M_\odot$ the luminosity function is likely to change in the following way. The faintest bins are likely to decrease in frequency as the number of contributing sources from fainter bins decreases with the majority of the model scenarios. The region of the luminosity function that is between H=14 and H=12 is likely to become steeper, with fewer sources in the fainter of these bins. We have not included these binary measurements in the modelling as the results rely on the interpretation of photometric measurements being accurate. Further measurements on the binary fraction in star-forming regions is required before this aspect implemented in the

code (e.g. the MONITOR project[3], which detects occultations in the light curves of young low-mass stars and brown dwarfs in open clusters and star-forming regions). Hydrodynamical simulations by Bate, Bonnell & Brom (2002) suggest that the binary fraction for brown dwarfs is ∼5%. If binary systems are in fact more prevalent for higher mass stars and the more massive brown dwarfs, this will have important implications when modelling the luminosity function. This scenario would mean that the faintest end of the luminosity function would remain approximately the same. The frequency of sources in the brighter of the intermediate bins will decrease, while the frequency of sources in the brighter bins will increase. For the best fitting functions this may produce a luminosity function that has a profile which is similar to that observed in Orion. However, the simulations by Bate, Bonnell & Brom (2002) produce only a small fraction of the number of sources we observe in Orion. In addition to this the limiting resolution of the model means binaries with very close separations cannot be formed. For this reason we have not tried to implement this result into the models.

8   SUMMARY AND CONCLUSIONS

A total of 40 of the sample drawn from this paper and Lucas et al.(2001;2006) show strong water absorption in their *H*- and/or *K*-band spectra. Some of these spectra also show evidence of CO absorption at *K*-band. We have developed a spectral typing scheme based on optically calibrated, near-infrared spectra of objects in the Taurus and IC348 star forming regions. These ranged from M3.0 to M9.5 in spectral type. Our spectral typing scheme showed that 23 of our objects had spectral types ranging from M4.0 - M9.5. A further 17 sources had very strong water absorption, indicating spectral types later than or equal to M9.5. Our calculated spectral types are accurate to within one sub-type for the majority of our objects. 12 sources in our sample have spectra that show clear Rayleigh-Jeans type continua. These are most likely to be reddened background stars.

The spectral type to effective temperature scale designed by Luhman et al. 2003 was used to calculate temperatures for each of our sources. We plotted the objects on an H-R diagram together with pre-main-sequence NextGen and Dusty isochrones and DM97 isochrones. The majority of the objects in our sample lie close to or above the 1 Myr isochrone suggesting an average cluster age that is ⩽1 Myr. Below 2500 K we see a population of objects that lie several magnitudes above the 1 Myr isochrone. This is in agreement with results by RRL. The position of these objects cannot be explained by unresolved multiple body systems or inaccurate distance measurements. This does not indicate a problem with calibrating sources from young objects in different clusters as a similar trend is observed at optical wavelengths. We do not observe an obvious population of objects 10 Myr in age.

We conclude from our results that the average cluster age is less than 1 Myr. We find that photometrically derived temperatures from the 1 Myr NextGen isochrone show fairly good agreement with spectroscopic measurements, but typically cooler by ∼100 K. We find that spectroscopic masses show a relatively poor agreement with photometrically determined masses. These findings are consistent with results from SCH04 and RRL.

We derive source masses from the H-R diagram that uses the combined NextGen and Dusty isochrones. 36 of the 40 sources plotted lie below the hydrogen burning limit (0.075 M⊙). The remaining 4 sources are low mass stars or lie close to the threshold. 10 of the 17 PMO candidates have masses that potentially lie below the deuterium burning limit (0.012 M⊙). If we use the models of DM97 the number of sources that lie below the hydrogen burning limit declines from 36 to 29.

We used a Monte Carlo approach to model the observed extinction limited luminosity function for the ONC. Our simulations show that single age distributions centred at 1 Myr with a narrow age spread fit the observed luminosity function best. A bimodal age distribution of 1 and 10 Myr sources also works well providing the respective ratio of sources is ⩾ 10 : 1. Broad singular age distributions generate too many sources in the intermediate luminosity bins and too few in the brighter bins. We conclude from our results that a continually rising star-formation rate as suggested by Palla et al. (2006 & 2007) is only plausible if it remained very low until ∼3 Myr ago. We find that a uniform age distribution produces a very poor fitting luminosity function. The best fitting version of the mass function is a Miller Scalo form at stellar masses that joins to an M$^\alpha$ power law for M⩽0.15 M⊙. Our most important result from the modelling is that planetary mass candidates are required to produce enough sources in the faintest magnitude bins. This holds true for scenarios that have bimodal age distributions with a moderate number of 10 Myr objects. A poorly fitting luminosity function is generated in every scenario where we truncate the IMF at the deuterium burning limit.

Although negatively skewed age distributions give the best results, we cannot definitively label it as the most appropriate age distribution. This is because the negative skew is best when it has a low dispersion and is centered at 1 Myr. A Gaussian distribution that has lower dispersion, centered at the same age would also approximate this result. A negatively skewed age population is significantly better than a Gaussian population at larger age dispersions. This is because it populates the intermediate bins of the luminosity function with fewer sources. The advantage of using a negatively skewed function for age is that it mimics a sudden burst in star formation that tails off over time. There seems to have been a sudden burst of star formation around 1 Myr ago in Orion. In most cases a positively skewed age distribution gave poor results. The only exception was for a 1 Myr population that has a low age dispersion.

[3] http://www.ast.cam.ac.uk/research/monitor/

9   REFERENCES

Allard F., Hauschildt P.H., & Schwenke D., 2000, ApJ 540, 1005

Allard F., Hauschildt P.H., Alexander D.R., Tamanai A., Schweitzer A., 2001, ApJ, 556,357

Baraffe I., Chabrier G., Allard F., Hauschildt P.H., 1998, A&A, 337, 403

Bate M. R., Bonnell I. A., Bromm V., 2002, MNRAS, 332, 65

Briceño C., Luhman K. L., Hartmann L., Stauffer J. R., Kirkpatrick J. D., 2002, ApJ, 580, 317

Breger M., Gehrz R. D., Hackwell J. A., 1981, ApJ, 248, 963

Burrows A. et al., 1997, ApJ, 491, 856

Cardelli J.A., Clayton G.C., Mathis J.S., 1989, ApJ, 345, 245

Cargile P.A., Stassun K.G., Mathieu R.D., 2008, ApJ, 674, 329

Chabrier G., Baraffe I., Allard F., Hauschildt P. 2000, ApJ, 542, 464

Comeron F., Rieke G.H., Burrows A., Rieke M.J., 1993, ApJ, 416, 185

D'Antona F., & Mazzitelli 1997, MmSAI, 68, 807 (DM97)

Gorlova N. I., Meyer M. R., Rieke G. H., Liebert J., 2003, ApJ, 593, 1074

Hillenbrand L.A., 1997, AJ, 113, 1733

Hillenbrand L.A., Carpenter J.M., 2000, ApJ, 540, 236

Hillenbrand L.A., Hartmann L.W., 1998, ApJ, 492, 540

Irwin J. et al., 2007, MNRAS, 380, 541

Jeffries R.D., 2007, MNRAS, 376, 1109

Kaas A.A., 1999, AJ, 118, 558

Kirkpatrick J. D., Barman T. S., Burgasser A. J., McGovern M. R., McLean I. S., Tinney C. G., Lowrance P. J. 2006, ApJ, 639, 1120

Köhler R., Petr-Gotzens M. G., McCaughrean M. J., Bouvier J., Duchêne G., Quirrenbach A., Zinnecker H. 2006, A&A, 458, 461

Levine J. L., Steinhauer A., Elston R. J., Lada E. A., 2006, ApJ, 646, 1215

Lodieu N., Dobbie P. D., Deacon N. R., Hodgkin S. T., Hambly N. C., Jameson R. F., 2007, MNRAS, 380, 712

Lucas P.W., Roche P.F., 2000, MNRAS, 314, 858

Lucas P.W., Roche P.F., Allard F., Hauschildt P.H., 2001, MNRAS, 326, 695L

Lucas P.W., Roche P.F., Tamura M., 2005, MNRAS 361, 211

Lucas P.W., Weights D.J., Roche P.F., Riddick F.C., 2006, MNRAS, 373, L60 (Paper 1)

Luhman K. L., Briceño C., Stauffer J. R., Hartmann L., Barrado y Navascus D., Caldwell N., 2003b, ApJ, 590, 348

Luhman K. L., Stauffer J. R., Muench A. A., Rieke G. H., Lada E. A., Bouvier J., Lada C. J., 2003, ApJ, 593, 1093-1115

Luhman K. L., 2004, ApJ, 602, 816

Luhman K. L., Peterson D.E., Megeath S.T., 2004, ApJ, 617, 565

Luhman K.L., Adame L., D'Alessio P., Calvet N., Hart-
mann L., Megeath S.T., Fazio G.G., 2005, 635, L93

Luhman K.L., Wilson J.C., Brandner W., Skrutskie M.F., Nelson M.J., Smith J.D., Peterson D.E., Cushing M.C., Young E., 2006, ApJ, 649, 894

Martín, E. L., Brandner, W., Bouy, H., Basri, G., Davis, J., Deshpande, R., Montgomery, M., King, I., 2006, A&A, 456, 253

Meeus G., & McCaughrean M.J., 2005, AN, 326, 977

Muench A. A., Lada E.A., Lada C.J., Alves J., 2002, ApJ, 573, 366

ODell, C. R., & Wen, Z. 1994, ApJ, 436, 194

O'Dell C. R., Wong K., 1996, AJ, 111, 846

Padgett D. L., Strom S. E., Ghez A. 1997, ApJ, 477, 705

Palla F., & Stahler S.W., 1999, ApJ, 525, 772

Palla F., Randich S., Flaccomio E., Pallavicini R., 2005, ApJ, 626, L49

Palla F., Randich S., Pavlenko Y.V., Flaccomio E., Pallavicini R., 2007, ApJ, 659, L41

Peterson D. E., Megeath S.T., Luhman K. L., Pipher J, L., Stauffer J. R., Barrado y Navascuès D., Wilson J. C., 2008, ApJ preprint doi:10.1086/'590527

Pinfield D. J., Dobbie P. D., Jameson R. F., Steele I. A., Jones H. R. A., Katsiyannis A. C., 2003, MNRAS, 342, 1241

Prosser C.F.F., Stauffer J.R., Hartmann L.W., Soderblom D.R., Jones B.F., Werner M.W., McCaughrean, M.J., 1994, ApJ, 421, 517

Reipurth B., Guimarães M., Connelley M., Bally J. 2007, AJ, 134, 2272

Riddick F., Roche P.F., Lucas P.W., 2007, MNRAS, 381, 1077 (RLL)

Rieke G.H., & Lebofsky M.J. 1985, ApJ, 288,618

Robin A.C., Reylé C., Derrière, Picaud S., 2003, A&A, 409, 523

Rodgers B., Wooden D. H., Grinin V., Shakhovsky D., & Natta A. 2002, ApJ, 564, 405

Simon M., Close L. M., Beck T. L. 1999, AJ, 117, 1375

Saumon D., Hubbard W. B., Burrows A., Guillot T., Lunine J. I., Chabrier G. 1996, ApJ, 460, 993

Siess L., Forestini M., & Bertout C., 1999, A&A, 342, 480

Slesnick C.L., Hillenbrand L.A., Carpenter J.M., 2004, ApJ, 610, 1045 (SCH04)

Stassun K. G., Mathieu R. D., Vaz L. P. R., Stroud N., Vrba F. J., 2004, ApJS, 151, 357

Tinney C. G., et al. 2004, Proc. SPIE, 5492, 998

Tout C. A., Livio M., Bonnell I. A., 1999, MNRAS 310, 360

Walker M. F., 1969, ApJ, 155, 447

Williams D.M., Comerón F., Rieke G.H., & Rieke M.J., 1995, ApJ, 454, 144

APPENDIX A: SPECTRAL TYPING DISCREPANCIES

The first anomaly in the spectral typing results can be seen in the QH_{UK} index for 013-306 (see Lucas et al. 2001 for H-band spectrum). The signal to noise of this spectrum is relatively high, resulting in a cubic spline fit that represents the pseudo continuum very well. It is therefore most likely that the index is not steep enough in the region of late-type objects to efficiently differentiate between spectral type. It

should be noted that no spectral index designed for this small wavelength range can be guaranteed to generate an accurate spectral type at all temperatures. This is because intrinsic scatter exists in the template data. This scatter is probably not attributed to the inherent low signal to noise of these objects, but to small differences in atmospheric structure and composition. Further cause for discrepancy may be attributed to dust or hot spots in the photosphere.

There is a discrepancy in both Q indices for the spectrum of 014-413 (see Lucas et al. 2001 for H- and K- spectra). The difference in the $QH_{(UK)}$ index is not obvious and is probably due to scatter in the index sequence as the signal to noise is relatively high. Over plotting template spectra revealed that H_2O absorption shortward of 1.675 µm is consistent with that of an object ranging from M8.0 - M8.5 in spectral type. However, the H_2O absorption on the red side of the triangular peak is weaker and more consistent with an object ranging from M4.0 - M5.0, thus skewing the $QH_{(UK)}$ result. The difference seen in the result of the $QK_{(UK)}$ index is likely to be due to decreasing signal to noise in the spectrum longward of the $\sim$2.2µm peak. The noise seems to be suppressing water absorption at the longest wavelengths, leading to a pseudo-continuum fit that makes 014-413 appear earlier in spectral type when using the $QK_{(UK)}$ index. This was confirmed by over-plotting the spectrum and pseudo-continuum fit onto template spectra. The result from the $QK_{(UK)}$ index was therefore not used to determine the final spectral type. The result from the $QH_{(UK)}$ index was not discarded as the quality of the spectrum is high.

The inconsistency that is present in the $QH_{(UK)}$ index for 015-319 is most likely due to low signal to noise in the H-band UKIRT spectrum for this object. Without sufficient signal to noise it is difficult to certify whether this discrepancy is purely down to the cubic spline fit poorly representing the real pseudo continuum. The template sample used for deriving the spectral typing scheme contains only two objects later than M9.0 in spectral type. It is therefore reasonable to assume the discrepancy in spectral type may be due to potential limitations in the QH index. Plotting template spectra on top of 015-319 clearly demonstrated that this object is later than M9.5

Results derived using the $K_{(UK)}$ indices provide less reliable results for the spectra of 068-019 and 069-209 due to poor signal to noise at K-band. The WK index for 095-058 produces a spectral type that is clearly later than those derived using the indices at H-band. A visual inspection of the spectra and cubic spline fits for this object reveal no obvious clue as to why there is a large discrepancy. The difference is most likely to be due to the profile of the K-band spectrum. We have investigated this possibility by superimposing template spectra of different spectral type on top of 095-058. This revealed that 095-058 does in fact appear later ($\sim$M9) at K-band, based on data shortward of the triangular peak. However, the water absorption longward of the peak is much weaker than seen in any of the late-type template spectra, despite the presence of multiple CO band-heads. This suggests that warm circumstellar dust may be present, resulting in a near-infrared excess. The UKIRT spectra were observed at a different epoch to the NIRI data. We can therefore not determine from this data whether the apparent difference in spectral type is due to short term spectral variability possibly caused by dust, or if the object is a spectrum variable

intrinsically different at K-band. Due to the strange nature of the spectrum beyond 2.26 µm we did not use the result from the QK index to determine a spectral type. We did use the result from the WK index as 095-058 does appear late over this wavelength region.

A further spectral typing discrepancy that is significant can be seen in the H-band indices for 186-631. This may be because the H-band spectrum for this object is of lower quality than the K-band spectrum. Careful inspection of this object indicates telluric noise may exist in the H-band spectrum at wavelengths < 1.58 µm. Plotting template spectra over the top of the spectra for this object demonstrated the derived spectral types were accurate. The consistent difference seen between H- and K-band is therefore not due to scatter in the indices. 186-631 has been observed at optical wavelengths by RRL, and assigned a spectral type of M8.0. This measurement strengthens the argument for telluric noise suppressing water absorption in the H-band spectrum. We were unable to test whether this is a reasonable diagnosis as an alternative telluric standard for 186-631 was unavailable. We can not rule out the possibility that this object has a spectrum that appears to be dissimilar at different wavelengths. For this reason all H- and K-band indices were used to spectral type this source.

APPENDIX B: SPECTRAL INDEX PLOTS

B1   UKIRT Indices

B2   GNIRS Indices

APPENDIX C: H-R DIAGRAM CONTAINING OBJECTS CALIBRATED FROM THE LODIEU SPECTRA
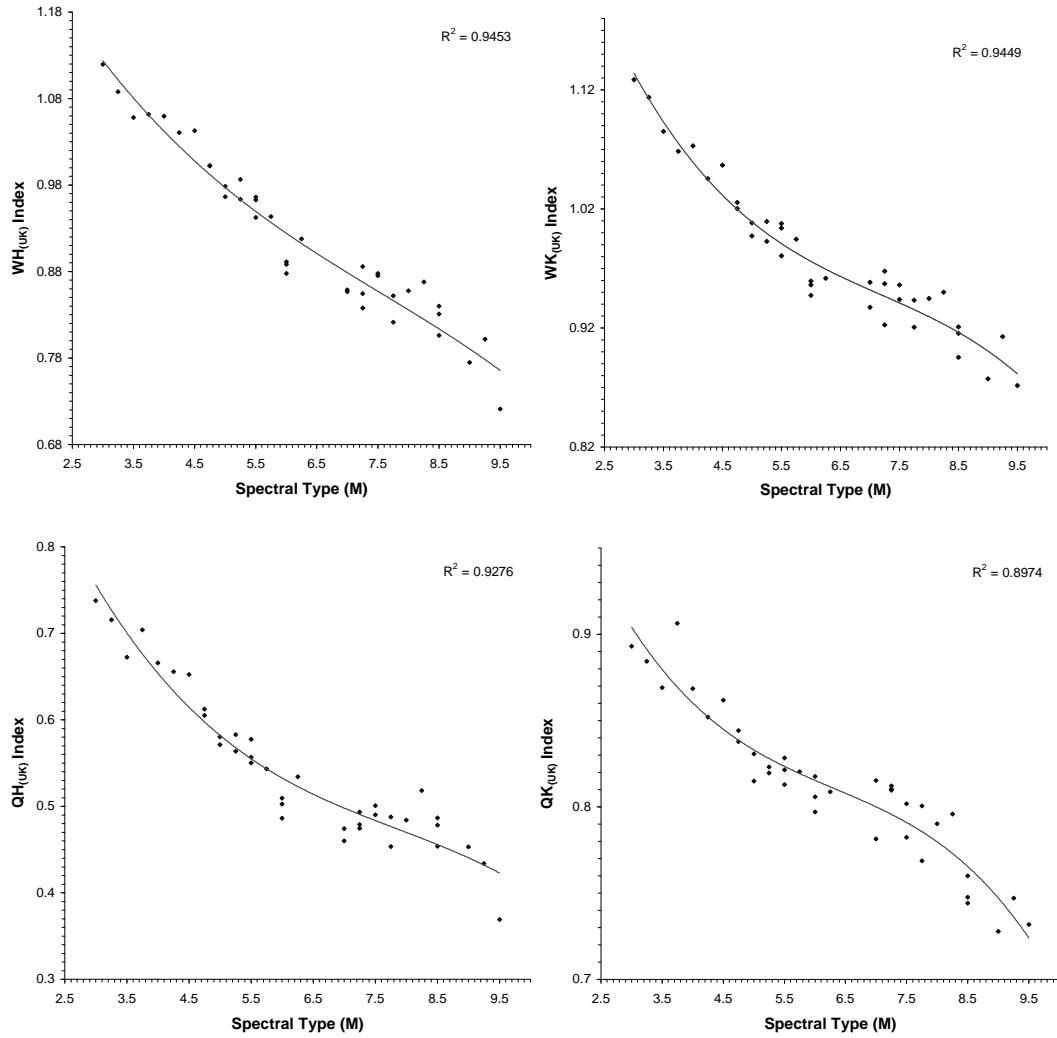
Figure B1. Fits to spectral indices used to characterise the UKIRT data. Index strength is plotted as a function of spectral type. Each data point represents an object from Luhman's near-infrared spectroscopic sample of optically calibrated young (∼1Myr) brown dwarfs. For each ratio the median flux value in a 0.02 μm interval was used. The relationship between spectral type and index are fitted by cubic polynomials. The R^2 values are correlation coefficients.
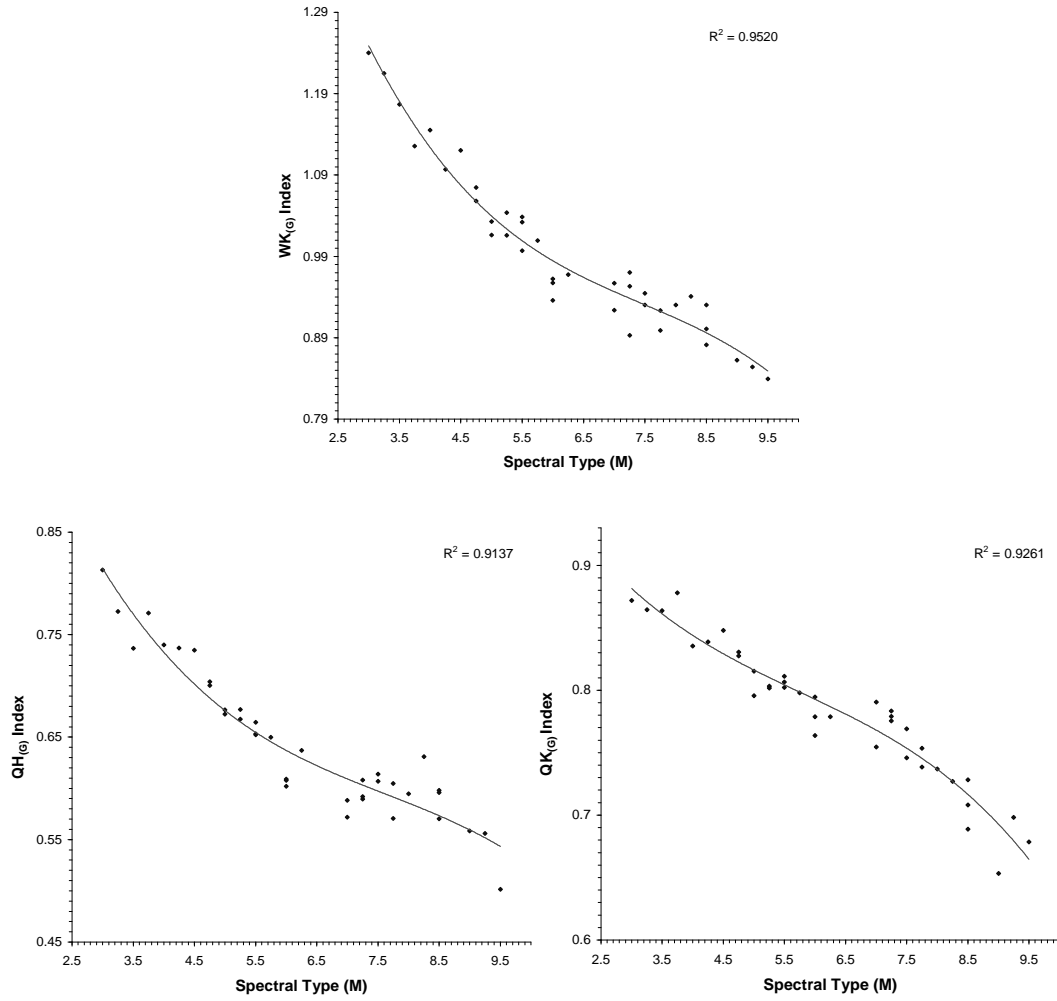
Figure B2. Fits to spectral indices used to characterise the GNIRS and NIRI data in Paper 1. Index strength is plotted as a function of spectral type. Each data point represents an object from Luhman's near-infrared spectroscopic sample of optically calibrated young (∼1Myr) brown dwarfs. For each ratio the median flux value in a 0.02μm interval was used. The relationship between spectral type and index are fitted by cubic polynomials. The R^2 values are correlation coefficients.
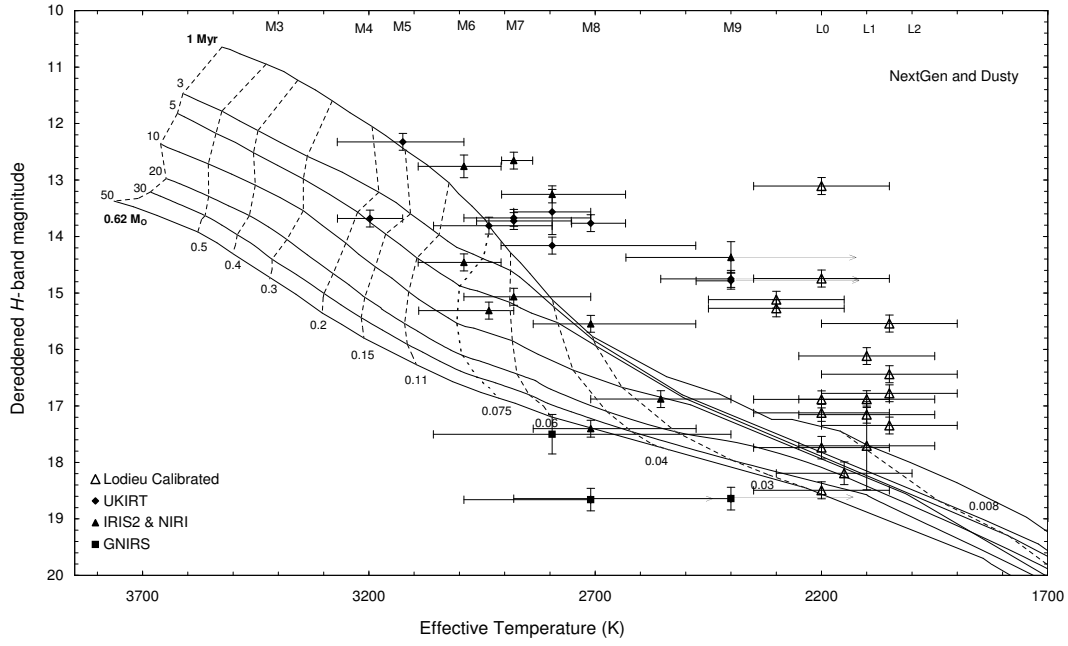
Figure C1. Sources calibrated from the Lodieu spectra are marked as open triangles. The pre-main-sequence tracks are from the NextGen and Dusty models. Temperatures were estimated from field dwarfs using data from Martín et al. 1999. Due to the fact that these values are estimated an error of ± 150 K has been used. The H-R diagram provides a reasonable estimate of the positions of these late M / early L-type objects.